Graz University of Technology

Bernhard Thaler, BSc

Ultrafast molecular photodissociation dynamics studied with single-pulse femtosecond photoelectron-photoion-coincidence spectroscopy

MASTER'S THESIS

to achieve the university degree of

Diplom-Ingenieur

Master's degree programme: Technical Physics

submitted to

Graz University of Technology

Supervisor:
Ass.-Prof. Dipl.-Ing. Dr. Markus Koch

Institute of Experimental Physics

Graz, March 2017

Affidavit

I declare that I have authored this thesis independently, that I have not used other than the declared sources/resources, and that I have explicitly indicated all material which has been quoted either literally or by content from the sources used. The text document uploaded to TUGRAZonline is identical to the present master‘s thesis.

Graz, _____ _____

Date Signature

Eidesstattliche Erklärung

Ich erkläre an Eides statt, dass ich die vorliegende Arbeit selbstständig verfasst, andere als die angegebenen Quellen/Hilfsmittel nicht benutzt, und die den benutzten Quellen wörtlich und inhaltlich entnommenen Stellen als solche kenntlich gemacht habe. Das in TUGRAZonline hochgeladene Textdokument ist mit der vorliegenden Diplombarbeit identisch

Graz, am _____ _____

Datum Unterschrift

Abstract

Ultrafast femtosecond photodissociation dynamics in isolated acetone molecules were investigated using femtosecond laser pulses of 400 nm. The pulses were obtained from second harmonic generation (SHG) of the 800 nm laser fundamental. The influence of different pulse parameters such as duration, positive/negative chirp, photon energy and pulse intensity on the photodissociation processes was studied. Self-Diffraction Frequency Resolved Optical Gating (SD FROG), a sophisticated autocorrelation technique for complete temporal characterization of the laser pulse electric field, was constructed and implemented in the setup. SD FROG has the additional advantage to measure femtosecond pulses independent of the laser wavelength.

Single pulse measurements on acetone were performed, where multiphoton excitation to high lying Rydberg states and single photon ionization happen within the same SHG femtosecond laser pulse. Different ionization channels could be identified using PhotoElectron-PhotoIon-COincidence (PEPICO) detection, where both the electron kinetic energy and the mass of the ionized molecule are measured at the same time. The kinetic energy of the electron identifies the species (parent or fragment) and the excited state from which the molecule is ionized. The ion mass in coincidence indicates if fragmentation happens. By varying the single pulse parameters like pulse duration ($100 - 200$ fs), photon energy ($2.99 - 3.18$ eV) and pulse intensity, a mechanistic picture of the ultrafast dissociation dynamics of acetone could be deduced. After Rydberg state excitation, electronic energy is redistributed to vibrational energy through non-adiabatic processes (internal conversion) on the timescale of the pulse duration, which causes the fragmentation of the molecule. Via the variation of photon energy, the activation energy to facilitate dissociation of the ionized acetone parent molecule to an acetyl and methyl fragment could be determined to be (0.79 ± 0.04) eV.

Kurzfassung

Es wurden auf der Zeitskala von Femtosekunden ablaufende Photodissoziationsdynamiken in Aceton-Molekülen in der Gasphase unter der Verwendung von Laserpulsen mit 400 nm untersucht. Die Pulse wurden per Frequenzverdopplung der 800 nm Laserfundamentalen erzeugt. Es wurde der Einfluss von verschiedenen Pulsparametern wie Pulsdauer, positiver/negativer Chirp, Photonenenergie und Pulsintensität auf die Photodissoziationsprozesse untersucht. Self-Diffraction Frequency Resolved Optical Gating (SD FROG), eine fortgeschrittene Autokorrelationsmethode zur kompletten zeitlichen Charakterisierung des elektrischen Feldes des Laserpulses, wurde konstruiert und in den Setup integriert. SD FROG bietet den zusätzlichen Vorteil, Femtosekundenpulse unabhängig von der Laserwellenlänge zu messen.

Es wurden Einpuls-Messungen an Aceton durchgeführt, bei denen die Multiphotonen-Anregung zu hochliegenden Rydberg Zuständen und die Einphotonen-Ionisation während der Dauer desselben Femtosekundenpulses auftreten. Verschiedene Ionisationskanäle konnten unter Verwendung der PhotoElektronen-PhotoIonen COincidence (PEPICO) Detektionsmethode, bei der die kinetische Energie des Elektrons und die Masse des ionisierten Moleküls gleichzeitig gemessen werden, identifiziert werden. Die kinetische Energie des Elektrons erlaubt die Identifizierung der Spezies (Parent oder Fragment) und des angeregten Zustandes, von dem das Molekül ionisiert wird. Die Masse des Ions in Koinzidenz erlaubt einen Rückschluss auf das Fragmentationsverhalten. Mittels einer Variation der Pulsparameter, wie Pulsdauer ($100-200$ fs), Photonenenergie ($2.99-3.18$ eV) und Pulsintensität, konnte eine mechanistische Modellvorstellung der Photodissoziationsdynamiken in Aceton abgeleitet werden. Eine Anregung von Rydberg-Zuständen setzt eine nichtadiabatische Umverteilung von elektronischer zu vibronischer Energie in Gang (Internal Conversion), welche auf der Zeitskala der Pulsdauern passiert und die Fragmentation bewirkt. Aus Messungen mit variabler Photonenenergie konnte die Aktivierungsenergie für verstärkte Dissoziation des ionisierten Aceton-Parent-Moleküls zu Acetyl- und Methyl-Fragmenten mit (0.79 ± 0.04) eV bestimmt werden.

Contents

CHAPTER 1

Introduction

Many fundamental processes in nature are a consequence of photochemical reactions. The initiated chemical mechanisms can happen on an ultrafast timescale on the order of picoseconds or even down to femtoseconds. For example, the photoisomerization process in the visual cycle that transforms the molecule retinal from a cis- to a trans-configuration, takes place with a time constant of approximately 200 fs [1]. Other famous examples are photosynthesis or the production of vitamin D.

There exist a variety of different photochemical processes. After the absorption of one or more photons, the electronic, vibrational and chemical structure of the absorbing species can be changed. The transferred energy will in general be redistributed via different mechanisms, including luminescence, dissociation, isomerization, charge transfer, as well as inter- and intramolecular energy transfer. A good summary and explanation of all these processes can be found in ref. [2]. The mechanisms that are most important for the results presented in this thesis are the dissociation of a molecule after intramolecular vibrational energy redistribution and subsequent ionization.

Because the very short time scales involved in these processes cannot be resolved or studied with conventional microscopic or spectroscopic methods, the new field of femtochemistry was established, which also led to the award of the Nobel Prize in Chemistry for Ahmed Hassan Zewail in 1999 [3]. Femtochemistry uses ultrashort laser pulses to investigate the dynamical processes, where the pulse durations are on the same order of magnitude as the time constants of the chemical processes. The pulses allow therefore a direct observation of the reaction. The most common method is to perform a pump-probe experiment, where

a pump beam induces some chemical dynamics that is probed with a second (probe) pulse afterwards for various time delays.

The experiments presented in this thesis were done in a laboratory that includes a commercial femtosecond laser system. The produced laser pulses can be used in pump-probe experiments as well as in single pulse studies, where the influence of the pulse parameters on the chemical processes are investigated. Isolated molecules in gas phase are excited and ionized and the transient species are measured with a time-of-flight (TOF) spectrometer. The setup allows a separate measurement of the emerging electrons and ions, as well as a combined study of both at the same time in coincidence, which is called PEPICO detection.

The concepts presented in the following chapter give some basic theoretical information for a better understanding of the results presented further down in chapter 3. Also some background information about the importance of pulse-duration measurements is given, which provides the basic for the setup presented in section 2.4.

1.1 Ultrafast photoexcitation dynamics: Basics

The fundamental processes which happen in a molecule after multiphoton excitation can be seen in figure 1.1. A molecule in the ground state absorbs one or several photons and gets excited to some (highly) excited state, in the case of figure 1.1 to a high lying Rydberg state (singlet, S_n). After the excitation, several processes start to happen, which in general take place at the same time: The additional absorption of another photon ionizes the species into the ionic ground state. The produced electron gains kinetic energy E_{kin}, which measured value can be be used to directly deduce the energy of the excited state E_{state}:

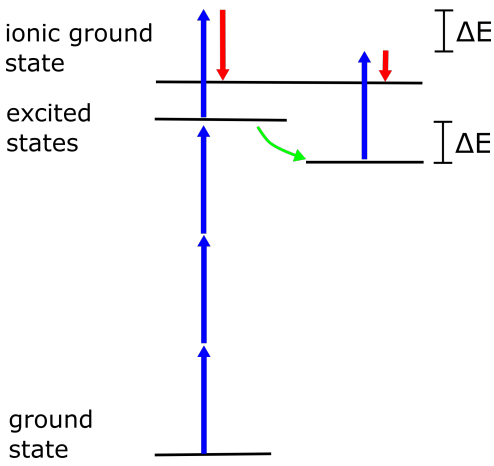

Figure 1.1: The basic process of multiphoton excitation, followed by one-photon ionization or relaxation into lower lowing excited states.

$$E_{kin} = E_{state} + E_{photon} - IP$$

(IP is the ionization potential). Such high lying states often undergo non-adiabative, radiationless relaxation to lower lying states. This relaxation process in figure 1.1 (green arrow) is however only visible in the depicted dimension and is basically a redistribution of energy

to other degrees of freedom, for example vibrational energies. There exist two possible mechanisms for such a change of electronic state plus intramolecular vibrational redistribution (IVR), that differ in the spin state that is populated through the conversion process [2]:

- **Internal Conversion (IC):** The transition is to a state with the same spin multiplicity, for example from a high lying singlet to an electronically lower, but vibrationally higher singlet.
- **InterSystem Crossing (ISC):** The transition is in principal spin forbidden for an optical transition, for example a singlet-triplet transition.

Both mechanisms have in common, that the transition takes place horizontally in the energy diagram, so no energy is redistributed directly, only afterwards the excess energy is lost, either through the emission of radiation or over radiationless vibrational deactivation. From the lower lying states, again photoabsorption causes ionization, with now lower kinetic energies of the electrons (see figure 1.1). In real systems, there exist of course a great variety of excited states, especially at high energies. From the peak positions in the photoelectron spectra, the populated excited states can be deduced and from the energetic distances, the amount of deposited energy ΔE can be calculated.

1.2 Probing photofragmentation processes with PEPICO detection

Because a significant amount of energy can be deposited to internal degrees of freedom (e.g. vibrations) during a relaxation process, this excess energy can cause the fragmentation of the molecule. For example, in the molecule acetone, which was investigated in the experiments done in this thesis, additional vibrational energy in the C-C stretch vibrational mode can cause the breakage of this bond and therefore lead to dissociation. In order to get information about this fragmentation process, the relaxation that leads to the energy deposition has to be investigated. Because the timescales of the processes are on the order of the pulse durations, a variation in pulse duration has to have an influence on the amount of fragmentation. Also the energy that is deposited into vibrations depends on the excited states that are populated in the beginning. A variation in the photon energy (excitation wavelength) should lead to the population of different states that also relax differently. Both approaches, the influence of the pulse length and the photon energy, were studied with the molecule acetone, the results are presented in chapter 3.
One standard method in femtochemistry is the measurement of transient photions and/or photoelectrons (see refs. [4] and [5]). However, the results with these techniques can be

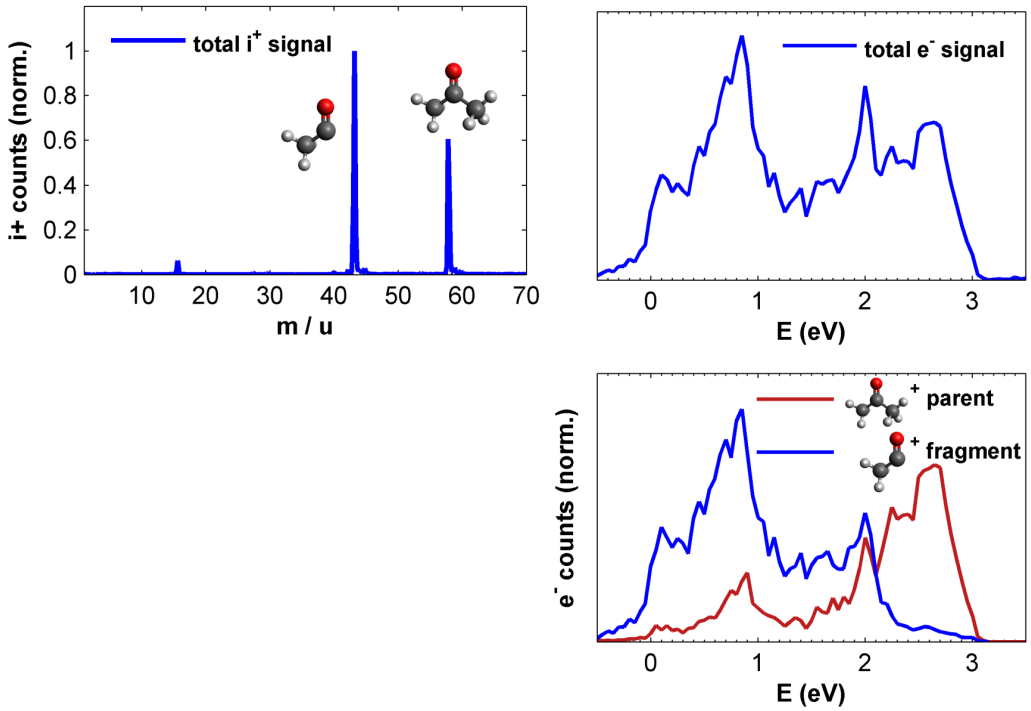

Figure 1.2: Typical photoion (upper left), photoelectron (upper right) and PEPICO (lower right) spectra of acetone after 400 nm multiphoton ionization.

misleading. An excellent tool to monitor fragmentation reactions in more detail is the measurement of electrons and ions in coincidence (PEPICO), measuring both species from the same ionization event and therefore be able to allocate photoelectron-spectra to every molecular fragment [6]. From the electron spectra, the electronic state before ionization and also the population of different ionic states can be identified. From the electron energy, the ionization channel (meaning the excited state before ionization, or also the ionized state that gets populated [7]) of the species can be identified and the appearance of such electron peaks in coincidence with a certain mass indicates the fragmentation behavior of the molecule. For example, if an electron peak is only measured in coincidence with a certain fragment and not in coincidence with the unfragmented parent molecule, the fragmentation has to happen before ionization and therefore in the neutral molecule after excitation [8]. Figure 1.2 shows in the upper images typical ion mass- and electron-spectra of acetone after multiphoton ionization. The lower right image shows the corresponding PEPICO spectra for the two major ion masses. From the single electron and ion mass spectra, one could conclude that the low electron kinetic energy peaks stem from states that led to fragmentation due to the higher energy deposition that happened in the relaxation process. However the PEPICO spectra show, that also unfragmented parent molecules are measured in coincidence with these electron energies and therefore not all molecules dissociate. Also for higher electron energies, fragment ions are measured,

however a clear edge for an increased acetyl signal is visible at around 2 eV (see lower right image in figure 1.2, blue curve). There exists a clear energy deposition threshold to facilitate the dissociation of acetone after a relaxation process. This is also evaluated and discussed in more detail in chapter 3.

1.3 Measuring ultrashort laser pulses

A very important parameter of ultrashort pulses is the pulse duration and the temporal or spectral phase distribution. A full characterization of an ultrashort pulse would be the knowledge about the full electric field E over time, meaning

$$E(t) = Re\{\sqrt{I(t)}exp(i\omega_0 t - i\phi(t))\}$$

where ω_0 is the carrier frequency and $\phi(t)$ is the time dependent phase, which contains the spectral distribution over time [9]. Especially when the spectral phase has terms that are of quadratic order (linear chirp) or higher (non-linear chirp), which is the general case, standard autocorrelation pulse measurement methods fail to give the correct pulse shape. More sophisticated techniques like FROG and SPIDER however provide the full information. Here a short overview over the different pulse duration measurement methods is presented.

Photodiode (= fast optoelectronic measurement):
With a high sampling rate, it can measure pulses down to approximately 10 ps, however only the pulse intensity is measured and no phase information can be retrieved.

Streak camera:
The pulse is periodically, rapidly deflected and the spatial signal is used to calculate the temporal width [10].

Optical autocorrelation:
The pulse is overlapped with itself in an interferometer and a corresponding higher signal around temporal overlap is used. The splitted pulses are overlappend for variable time delays τ and the resulting signal is measured, no fast responding photodiode is needed. There exist several methods which are briefly discussed in the following, they all have in common, that the temporal pulse form $E(t)$ cannot be retrieved completely and especially for chirped pulses the results can be misleading.

- *Field autocorrelation:* The autocorrelator consists basically of a Michelson Interferometer, where the pulse is splitted into two beams, that are delayed with respect

to each other and then collinearly overlapped to measure the interfered signal for variable time delays. The signal is recorded with a photodiode and is proportional to the following form:

$$A(\tau) = \int_{-\infty}^{+\infty} |E(t) + E(t-\tau)|^2 dt$$

As can be seen in figure 1.3 b), the field autocorrelation clearly underestimates the pulse duration for a chirped pulse due to the loss in coherence because different frequencies overlap. One could also say, that the chirped pulse contains more bandwidth and therefore the field autocorrelation is shorter due to the constant time-bandwidth product [11].

- *Intensity autocorrelation:* The splitted pulses are non-collinearly overlapped in a non-linear crystal to enable second harmonic generation (SHG). Frequency doubled light that is produced at temporal overlap leaves the crystal at a normal angle because of momentum conservation. The retrieved signal has the form:

$$A(\tau) = \int_{-\infty}^{+\infty} I(t)I(t-\tau)dt$$

Note that because not the electric field but rather the intensity, which is the absolute square of the electric field, goes into the term for the autocorrelation signal. Therefore, the pulse width is retrieved correctly for chirped pulses, however there is no information about the phase distribution, which is shown in figure 1.3 c) [11]. A so called single shot autocorrelator (SSA, Coherent) is at hand in the laboratory, which maps the temporal overlap profile of the pulse on a spatial intensity curve of the generated second harmonic. It can however only be used for pulses with 800 nm (phase matching sensitivity of the non-linear crystal, compare section 2.3) [12].

- *Interferometric autocorrelation:* Here a combination of the two previous methods is used. A collinear autocorrelator produces an overlap in a SHG crystal. The signal recorded is:

$$A(\tau) = \int_{-\infty}^{+\infty} |(E(t) + E(t-\tau))^2|^2 dt$$

Note that again the order of the process is the E-field powered with four (due to second harmonic generation), however the phase of the E-field influences the magnitude of the signal. In figure 1.3 d) it can be seen, that the autocorrelation width of the chirped pulse is again more narrow, however some fringes exist that hint a non uniform phase distribution [11].

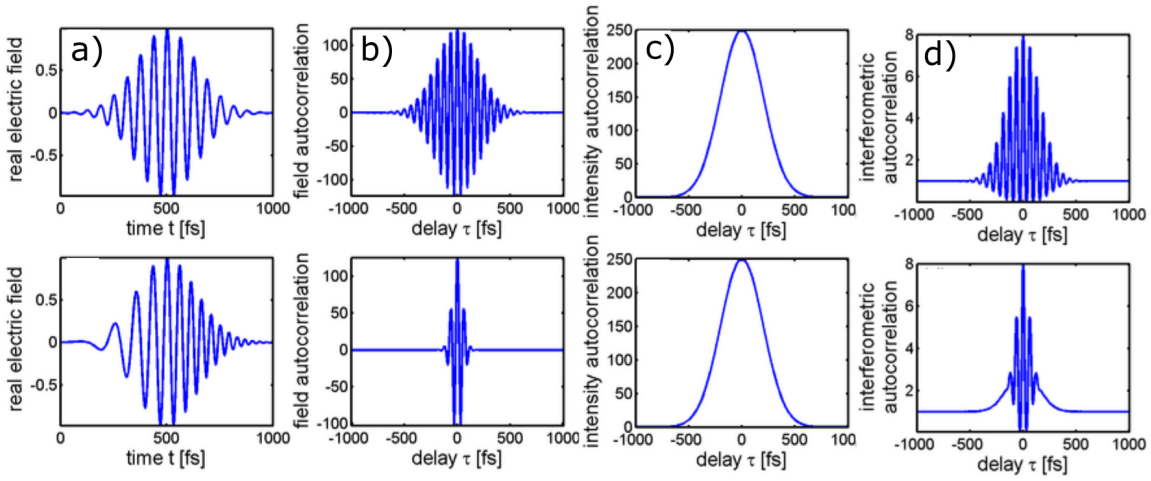

Figure 1.3: The autocorrelation spectra for an unchirped (upper a) and a linearly chirped (lower a) pulse with same pulse widths for the field autocorrelation b), the intensity autocorrelation c) and the interferometric autocorrelation d).

FROG:

A setup that uses a frequency resolved autocorrelation signal is called a FROG (Frequency Resolved Optical Gating) autocorrelator. There exist several types, depending on the autocorrelation signal that is used (e.g. Self Diffraction, SHG, THG, Transient Gating TG). They all have in common, that the autocorrelation signal is a two-dimensional function depending on the wavelength/frequency and the time-delay [9]. Out of this so called FROG trace, the real electric field can be calculated via iterative retrieval algorithms. A Self-Diffraction FROG was set up in the working period of this thesis and is described in more detail in section 2.4.

SPIDER:

Another frequently used technique for complete ultrashort pulse characterization is spetral phase interferometry for direct electric field reconstruction (SPIDER). Here a beam is again split, delayed temporarily and the two pulses are introduced to a frequency shift with respect to each other. This is done with sum frequency mixing (SFM) of the two pulses with a part of the original pulse that is broadened widely in a dispersive medium. The retrieved signal is recorded for various time delays and with a Fourier-based reconstruction algorithm the true pulse form is calculated [13].

CHAPTER 2

Experimental

The experiments presented in this thesis were started on a setup which partly already existed at the beginning of the working period and which is described in the master theses of Paul Maierhofer [12] and Markus Bainschab [14]. Parts of the components, especially of the optical setup, were modified and changed to fit the requirements for the measurements which are presented in chapter 3:

- The data acquisition methods, especially the software algorithms, were improved and extended, see sections 2.2 and B.1.
- Second Harmonic Generation was introduced on a more sophisticated level and methods to alter the wavelength of the frequency doubled light were tested, see section 2.7.
- A Self-Diffraction Frequency Resolved Optical Gating (SD FROG) setup for ultrashort pulse duration measurements was introduced and characterized, see section 2.4.
- Methods to change and characterize ultrashort pulse parameters (wavelength, duration, chirp and energy) were established. This gave the experimental basis for measurements to investigate the influence of the pulse parameters on the fragmentation behavior of isolated molecules, which where performed using PEPICO spectroscopy. The results are presented in chapter 3.
- An Optical Parametric Amplifier (OPA) was introduced in the laboratory and characterized. Measurements regarding the output stability and an optimal configuration were performed (see section 2.7).

2.1 Overview

The setup consists of a commercial femtosecond laser with amplification system, an optical table with various optical components and of a time-of-flight spectrometer, in which the investigation of the desired species (e.g. molecules) takes place and the data is collected. An overview of the setup is shown in figure 2.1.

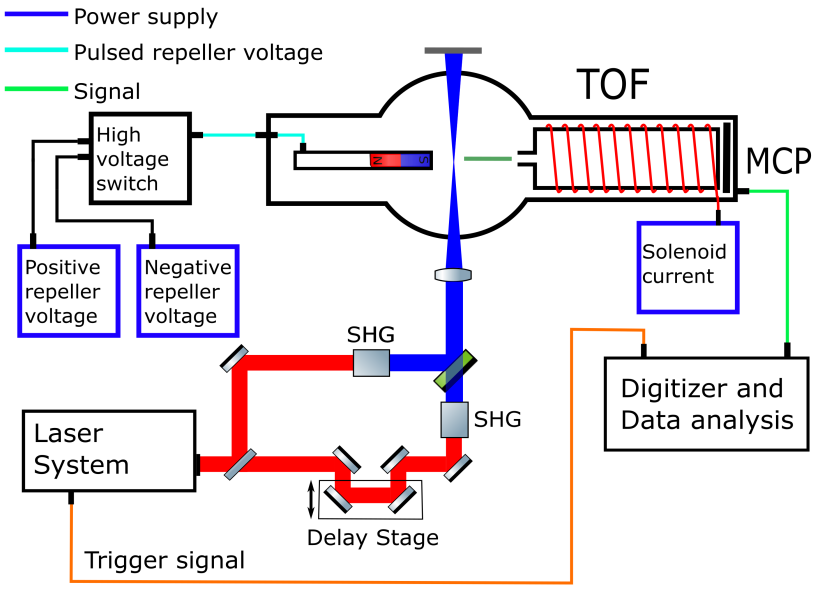

Figure 2.1: Basic setup for time-resolved experiments, consisting of the laser itself, optical components for frequency doubling and the time-of-flight spectrometer. As explained in the text, only one path is used for single pulse experiments in this thesis.

The fundamental of the laser is frequency doubled and focused into the chamber and the molecules inside are electronically excited and ionized by the laser light. The created ions and/or electrons are collected by the time-of-flight (TOF) spectrometer and are evaluated with respect to their mass and energy, respectively. Hereby spectra of ion masses and electron energies are retrieved, which allow the investigation of electronic structure. The setup can be used to study ultrafast dynamics in the species by performing a pump-probe experiment. A pump pulse excites the molecule and introduces a dynamical process which can be probed by a second ionization pulse at specific (femtosecond) time delays. However, the experiments described in this thesis concentrate mainly on one-pulse measurements, where the excitation and the ionization of the molecule happen within the duration of a single pulse. It is shown, that also with a change of the pulse parameters like photon energy, pulse duration or pulse energy, specific insights into the dynamics in a molecule can be derived from single pulse experiments.

2.1.1 Optical setup

Laser pulses are delivered by a commercial Ti:sapphire laser of Coherent (Vitara oscillator) and a dual stage chirped pulse amplification system (Legend Elite Duo). The system has a repetition rate of 3 kHz with an averaged output power of about 13 W with a nominal pulse length of 25 fs. The vertically polarized output pulses have a central wavelength of 800 nm with a bandwidth of about 80 nm.

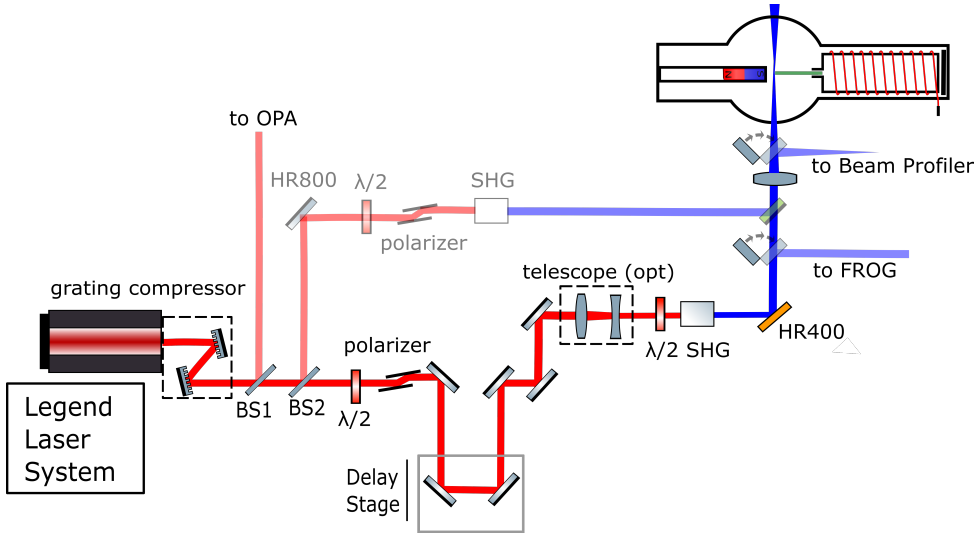

Figure 2.2: Elements of the optical setup. The opaque beam path (reflected part after BS2) was not used in the experiments described in this thesis.

The important parts of the optical setup can be seen in figure 2.2. With a beamsplitter right after the exit, the main pulse (reflection: 80%) of the output power can be used for the Optical Parametric Amplifier (OPA, see section 2.7). The transmitted pulse is again splitted with a second beamsplitter (BS Newport, part number: 20RQ00UB.2, reflection: 30%) and the two remaining beam paths can be used separately for one-pulse measurements or in combination in a pump-probe experiment (see ref. [12]), where the probe pulse is delayed with respect to the pump pulse over a delay stage. In the experiments described in this thesis, only the path over the delay stage (the stage has no influence) was used, pump-probe experiments with SHG in both pathways are described in the master thesis of Pascal Heim [15]. After the beam splitter BS2, a half-wave plate in combination with two Brewster windows gives the possibility to manipulate the pulse energy (see section 2.6). Following the polarizer, the again vertically polarized beam with the fundamental wavelength (800 nm) is rotated 90° by a half-wave plate in order to fulfill the phase-matching condition of the frequency doubling BBO crystal afterwards. A detailed description of frequency doubling and manipulation of the phase-matching is given in section 2.3. Right after the BBO, a dichroic mirror (HR400) separates the second

harmonic from the fundamental. The light is then focused into the measurement chamber with a plano-convex 500 mm CaF_2 lens, which has a high transmission from the infrared deep into the ultraviolet. Before and after the lens, flipper mirrors can be inserted in order to measure the important beam parameters. The first flipper (before lens) introduces an UV enhanced aluminum mirror (Thorlabs), which guides the beam into a Frequency Resolved Optical Gating (FROG) autocorrelator (see section 2.4). The second mirror (again aluminum, Thorlabs) guides the focused beam to a homemade beam profiler, to measure the spatial profile of the focus (see bachelor thesis of Christian Goesweiner [16]).

2.1.2 Measurement chamber and time-of-flight spectrometer

Over a CaF_2 window, the focused beam is guided into the main vacuum chamber. With a dosing valve, a desired gaseous species (in the case of the measuerments in this thesis: acetone) can be introduced over its vapor pressure to the chamber, which has ultra-high vacuum base pressure ($\approx 1 \cdot 10^{-10}$ mbar). The molecules are ionized at the laser focus and electrons and/or ions can be collected with the time-of-flight (TOF) spectrometer, where the desired particles are pushed into a tube and detected with a Multi Channel Plate (MCP) detecter of type chevron at the end of the drift tube (see figure 2.1). A detailed description of the design of the spectrometer and the different measurement modes can be found in the master thesis of Markus Bainschab [14] and the bachelor thesis of Franz Koberg [17]. Here only a short summary is presented:

- **Electron mode:** A small negative voltage (-3 V) on a magnetic repeller in front of the laser focus pushes the electrons into the drift tube. The magnetism of the repeller, in combination with the magnetic field of a solenoid around the tube (a so called magnetic bottle) increases the number of electrons entering the tube. Over the measured flight-time, the kinetic energy of the electrons can be determined.

- **Ion mode:** A positive high voltage (2000 V) pushes the ions into the tube and their flight-time is used to determine their mass. No magnetic field is applied, since it has no big influence on the heavy ions.

- **PEPICO mode:** In this mode, PhotoElectrons and PhotoIons are detected in COincidence, meaning that both voltages are applied to the repeller consecutively. At first, the very fast electrons are detected and afterwards a high voltage pulse (2000 V) pushes the remaining ions to the detector. A High Voltage switch is responsible for the fast switching between the voltages.

2.1.3 Data acquisition

The electrons and ions hit the dual stage MCP detector and generate an electron avalanche due to a high potential difference, which is realized with three voltages: a small positive front voltage of 45 V, a high positive back voltage of 2100 V and a high voltage at the phosphor screen of 2500 V. The analog electric signals of the electron/ion hits are decoupled from the phosphor and are either guided to a scope or are digitized with a high speed analogue-to-digital converter (GaGe Cobra 2GS, 500 MHz bandwidth) and are evaluated at the PC. With software algorithms, the hits are detected and statistically evaluated, which is described in more detail in section 2.2.

With the PEPICO detection algorithm, only those hit events are considered, where one electron and one ion hit are detected during the same time trace, which corresponds do the signal after one laser shot. When the general number of events per laser shot is low, which can be controlled either by the laser power or the vapor pressure, it can be assured, that the majority of ions and electrons that are detected in coincidence stem from the same ionization event [18]. However, the fraction of coincidences will be very low compared to for example single ion hits or single electron hits and therefore long measurement times are necessary in order to get good statistics. A main advantage of the PEPICO method is the clear identification of fragmentation channels before or after ionization. From the histograms in the time frame, the electron kinetic energy spectra can be calculated for each ion mass that was detected.

2.2 Retrieving and evaluating time traces of the TOF spectrometer

In order to get the highest information out of the collected data, it is important to understand the data acquisition process. A hit generates a voltage pulse at the MCP, which is amplified with a fast timing pre-amplifier (Ortec VT120, either +200, -200 or +20 db) and at the end of the data cable again attenuated with a BNC attenuator (Telegärtner J01006A08, 20 db) in order to reduce noise. Hits are detected either with the scope in combination with a counter, or digitally over the digitized time trace (GaGe card) and can then be statistically stored in histogram files. The focus in this chapter lies on the handling of the retrieval of a hit in a digitized time trace and explains the basics that are necessary for the code, which is realized in the program *RMT_v2* (Record Multiple Traces version 2) and its subprograms *findpeak.c* and *writefile.c*. The handling and the principle of these programs are explained in Appendix B.1.

2.2.1 Time trace shape

The MCP produces a continuous analogous signal. A time trace is defined as this signal from the starting point at the moment when a laser pulse leaves the amplifier (every 1/3000 = 0.33 ms) plus a specific delay until 10 or 20 μs, depending on the sampling rate of the digitizer. The maximum sampling rate is 2 GS (GigaSamples) per second, meaning that two data points are recorded for each nanosecond. This was the standard sampling rate for the experiments presented in this thesis. The starting point for each time trace (meaning the moment the laser leaves the amplifier) is taken from a trigger signal of the laser itself, which gives a 3 kHz square wave signal. A typical time trace recorded with 2 GS can be seen in figure 2.3.

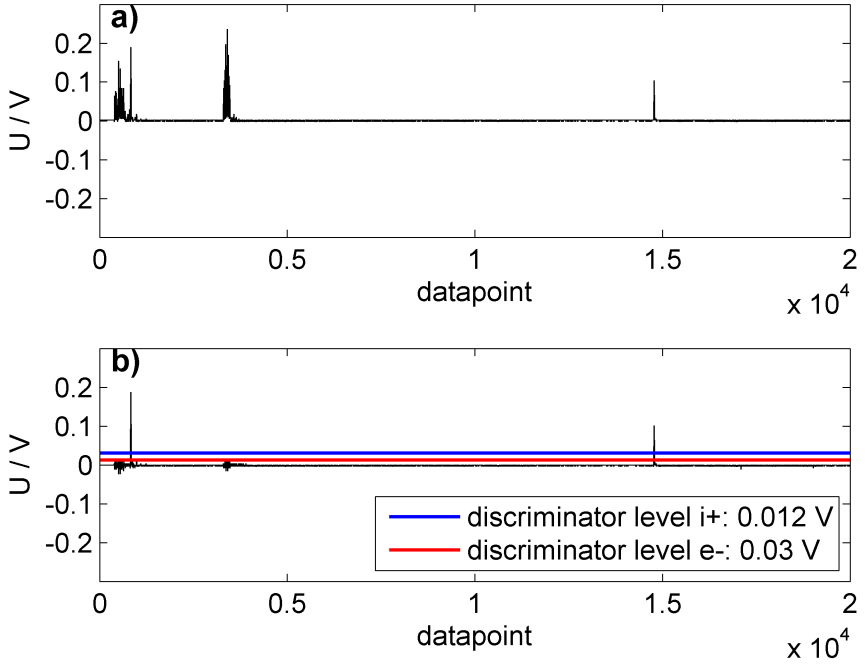

Figure 2.3: A typical 2 GS (10 μs) timetrace with a coincidence hit of one electron and one ion. The top image a) shows the raw data, the bottom image b) shows the raw data subtracted by the mean data of the last 100 measurements.

The top image a) shows the raw data time trace. Note that the datavector contains $2{\cdot}10^4$ datapoints, which gives with a sampling rate of 2 GS a time trace of 10 μs. The time trace visible in figure 2.3 was taken in PEPICO mode. At two time points, at first shortly at the beginning and second at around 2200 ns (4400 in datapoints), a high noise signal is detected. This is due to the switching (on and off) of the high voltage, which induces currents in the flight tube of the spectrometer and also a signal in the MCP [14]. Between the noise signals, a signal peak is visible, which is caused by a (faster, and therefore

earlier) electron. The peak that appears later is due to the ion, that has a much higher mass and therefore a lower kinetic energy.

2.2.2 Constant Value vs. Constant Fraction Discriminator

In order to detect the peaks as a hit, one has to define a discriminator level, which has to be overcome from the signal. Figure 2.3 b) shows typical values for the discriminator. The level for the ion detection can be set very low due to the absence of noise signals. However for electrons, especially the first noise signal is a problem, because it appears where electron hits should be detected. The discriminator would have to be set very high. A good method to overcome this problem, is to always average the last 100 time-traces (in which no hits were detected) and subtract them from the raw data time trace. In figure 2.3 b) it can be seen, that the noise signal nearly vanishes and the discriminator level for the electrons can be set much lower than the original noise level, hence the electron detection efficiency can be increased significantly.
There are two main strategies to detect the position of a peak:

- **Constant Value Discriminator CVD:** A peak is detected, if the voltage value is higher than a given threshold.

- **Constant Fraction Discriminator CFD:** A peak is detected, if the slope of the peak (the difference of the trace with itself, shifted by one or two timesteps) is higher than a given threshold. This has the advantage, that peaks of different height are always detected at the same position.

Because of a given width of the pulses, a hit is stored 2 ns after the discriminator is overcome. The preferred method during the experiments done in this thesis was CVD, because of its easier handling and understandability. Due to the low energy resolution caused by the spectral broadness of the laser itself, the gain of CFD over CVD with respect to precision played no important role.

A common problem in this context is the appearance of double peaks due to reflections in the data cable. A voltage pulse gets reflected back at the digitizer and again at the MCP and can be detected another time as a peak in the algorithm, if it is high enough for the set discriminator. In this case, a single hit would be detected as two or even more. To avoid this problem, a non constant discriminator is introduced. If a hit was detected, the discriminator level is set to a higher value, e.g. from 0.03 V to 0.15 V for the electrons for a certain time period (usual value: 100 ns). It was found, that the disadvantage of losing real electron hits during this time has only minor influence.

2.2.3 Data storage

Once a hit is detected, it is stored separately in two .txt files (see appendix B.1 for the code):

- **Hist File:** This file has as number of rows/lines the number of time datapoints, so for 2 GS it contains $2{\cdot}10^4$ lines. In each row the number of hits, that appeared at that timestep, is written. The hist file is the histogram file of the spectrum in the time frame.

- **List File:** The list file stores the hits for every shot of the laser, so for a typical measurement with $1{\cdot}10^6$ shots it also has $1{\cdot}10^6$ lines. The first column contains the number of the shot, the second the number of hit events after this shot and the following columns list the datapoints, at which these events happened.

Both file types are generated for each measurement for electrons, ions and for both electrons and ions (for PEPICO evaluation). The difference between electrons and ions is set manually by the time, the high voltage is turned on and off. Also during the period where the voltage is turned off (second noise signal), data collection is excluded because no electrons or ions will in general be detected in this region.

2.3 Second Harmonic Generation and λ variation

Three β-barium borate (BBO) crystals of different thickness have been used to create the second harmonic of the 800 nm fundamental (listed in table 2.1).

Table 2.1: SHG crystals used in the laboratory

name	number	phase matching
SHG BBO Crystal 100 μm	BTC5010-SHG800(I)-AR	type I
SHG BBO Crystal 200 μm	BTC5020-SHG800(I)-AR	type I
SHG BBO Crystal 500 μm	BTC5050-SHG800(I)-AR	type I

All of the crystals use type I phase matching (cut angle $\phi = 29.2\ °$), meaning that two horizontally polarized fundamental photons produce one of the second harmonic that is vertically polarized. A thicker crystal gives a better conversion efficiency, hence a lower fraction of the fundamental, but due to a higher group delay dispersion also longer temporal pulses. Also a thicker crystal is more sensitive to the phase-matching condition, therefore giving a more narrow bandwidth of the frequency doubled pulse. In order to fulfill this phase matching condition:

$$
\begin{array}{ccccc}
\mathbf{k}_1 & + & \mathbf{k}_1 & = & \mathbf{k}_2 \\
\mathrm{n}(\omega_1)\omega_1/\mathrm{c} & + & \mathrm{n}(\omega_1)\omega_1/\mathrm{c} & = & \mathrm{n}(\omega_2)\omega_2/\mathrm{c} \\
 & & 2 \cdot \omega_1 & = & \omega_2 \\
 & & \mathrm{n}_o(\omega_1) & = & \mathrm{n}_{eo}(\omega_2)
\end{array}
$$

the electric field polarizations of the fundamental and the second harmonic have to be chosen, that they propagate as an ordinary (n_o) and an extraordinary (n_{oe}) beam of a birefringent crystal. Then the indices of refraction are different and the phase difference due to dispersion effects can be compensated.

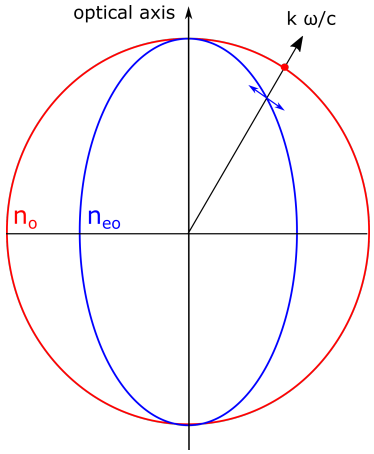

Figure 2.4: Different indices of refraction for a negative uniaxial birefringent crystal. The blue line marks the extraordinary beam, with a partial polarization in the direction of the optical axis. The red line marks the ordinary beam, with the polarization direction always orthogonal to the optical axis. Changing the propagation direction (vector k) also changes the frequencies, for which the phase matching condition is fulfilled.

When the crystal is tilted or rotated, the phase matching condition is altered due to a change in the e.o. index of refraction because its beam polarization is now more or less parallel to the optical axis (compare with figure 2.4). If the fundamental was purely monochromatic, no second harmonic light at all would be created when the crystal angle is not at the optimum position. However, since the laser fundamental in the laboratory has a bandwidth of approximately 80 nm, the tilting/rotation of the crystal changes just the part of the fundamental spectrum that is frequency doubled. This turned out to be a good method to scan the SHG wavelength. However, a limit to this is the minimum pulse length, which turned out to be quite high, to get a reasonable SHG bandwidth (the reason for this remains unclear at the moment). With the loss in intensity of longer pulses, also the conversion efficiency drops and therefore the intensity of the desired wavelength decreases, while the intensity in the fundamental (800 nm) increases.
A normal procedure would be a tilting with simultaneous rotation of the crystal while

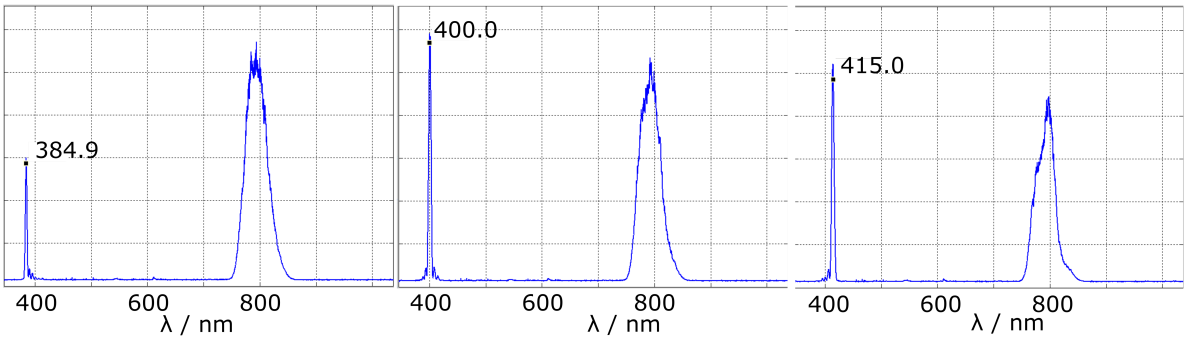

Figure 2.5: Three different wavelengths of the second harmonic, achieved by aligning the crystal axes.

monitoring the output spectrum with a spectrometer. An optimal spectrum would have a high intensity in the desired wavelength and the fundamental as low as possible, guaranteeing a high conversion efficiency. With the 500 μm BBO, a wavelength variation between 385 to 415 could be achieved, with moderate fundamental parts at the edges of this SHG bandwidth (see figure 2.5). It should be noted, that for the spectra in figure 2.5 also a dichroic HR400 mirror was placed after the BBO, which also decreases the intensity of the fundamental (see figure 2.2). A good improvement of the conversion efficiency (especially at wavelenghts away from the fundamental SHG) could also be performed with the introduction of a telescope before the BBO (see figure 2.2), reducing the spot size and therefore having higher intensities in the center of the BBO. For example, a telescope with a focus length ratio of

$$f_1/f_2 = 50 \text{ mm} \ / \ 20 \text{ mm} = 2.5$$

also reduces the spot size by a factor of 2.5. However, the additional material of lenses has also an effect on the pulse length due to dispersion effects, so the introduction of a mirror telescope might be the more favourable choice.

2.4 Self-Diffraction Frequency Resolved Optical Gating - SD FROG

When working with ultrashort pulses, it is of course essential to get a profound knowledge about the exact pulse duration and the distribution of its spectral phase (compare chapter 1). A Frequency Resolved Optical Gating (FROG) apparatus is an autocorrelator with a frequency resolved autocorrelation signal. There exist various methods for introducing that signal, for example via second harmonic generation (SHG FROG), via a gating over

polarization change (PG FROG) or via the diffraction on a non-linear grating generated by the pulse itself (SD FROG) or by a third pulse (TG FROG). The different FROG types, the evaluation of a FROG trace and the retrieval algorithm are very well described by Rick Trebino in ref. [9]. In this laboratory an autocorrelator of the type Self-Diffraction Frequency Resolved Optical Gating, short SD FROG, was set up and characterized during the working period of this thesis.

2.4.1 Setup and principle of operation

The schematic setup of the SD FROG is shown in figure 2.6 and an image of the real apparatus is depicted in figure 2.7. The whole setup is mounted on a separate optical plate, which allows a flexible alignment. The laser is coupled into the FROG via a flipper mirror and is guided to an ultrathin beamsplitter (BS) of type Pellicle (Thorlabs BP108, Uncoated for 8:92 (R:T)). The beamsplitter is hit with a very high incidence angle because of the otherwise too low reflected intensity, which should be in the best case as high as the transmitted one. The reflected beam is guided over a delay stage and is again spatially overlapped with the transmitted beam in the focal plane of a 100 mm lens (L1). In the plane, a thin and transparent optical medium is placed, which favors a $\chi(3)$ effect (Non Linear Medium - NLM). In the current setup, a thin cover slip (normally used in microscopy) is used. A more favorable material would be fused silica, due to a lower fraction of stray light especially at lower wavelengths (e.g. around the SHG of 400 nm). In this material the SD-FROG magic happens: if the beam paths have identical lengths, the pulses also temporarily overlap and produce a constant intensity modulation, similar to a standing wave. Because of the non-linear optical Kerr effect, which describes an intensity dependent refraction index, a grating with alternating high and low refraction indices is formed. On this grating the pulses itself are ('self-')diffracted and the intensity of the diffracted beam forms the autocorrelation signal. It is guided over a second lens (50 mm, L2) into a glass fiber and a spectrometer (model OceanOptics USB4000+), where it is spectrally resolved. A temporal scan (movement of the stage) of the diffracted beam spectrum is recorded and the two-dimensional signal map, meaning the intensity over wavelength and time delay, forms the so called FROG trace. Also, the non-spectrally resolved autocorrelation function is obtained as a by-product. From the two-dimensional FROG trace, the real pulse shape and its phase distribution can be calculated with a separate retrieval algorithm, which is described in more detail in ref. [9]. The main advantage of the SD FROG is the wavelength-independence of the pulse to be measured and therefore a very wide usability.

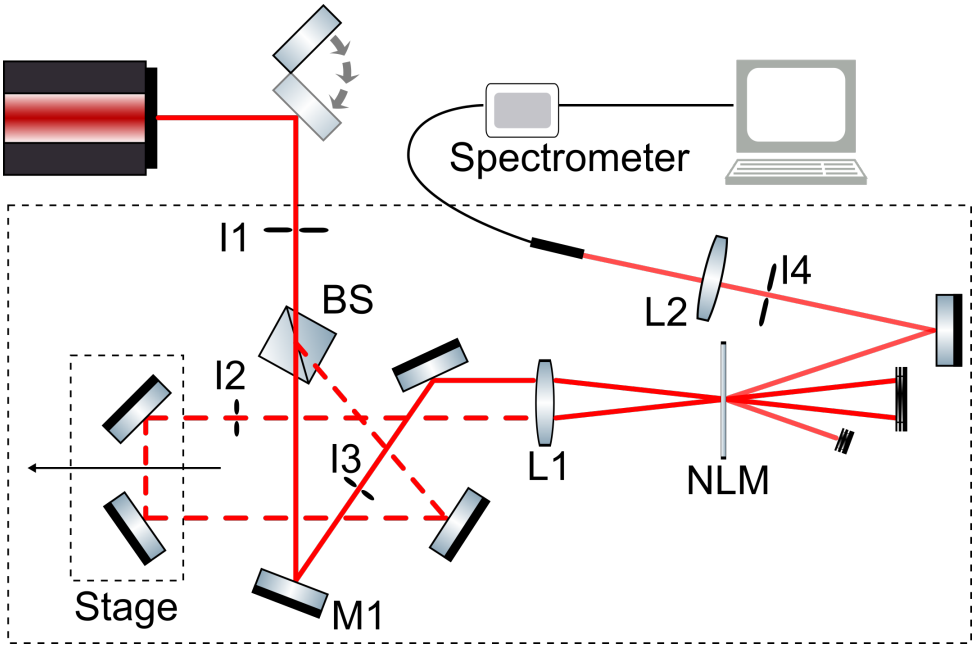

Figure 2.6: Schematic setup of the Self-Diffraction FROG autocorrelator. Note that because of aesthetic reasons, the two beam paths do not have the completely same length here.

2.4.2 Taking and retrieving a FROG trace

Here a brief description of how to couple a short pulse into the FROG apparatus, how to get to the autocorrelation signal and how to record a FROG trace of good quality is given.

- **Step 1: Coupling the beam**.
  The beam path in the FROG (and also before the apparatus) should always be well documented, in order to perform a fast signal generation. In the laboratory, the iris apertures I0 (not visible in figure 2.7) and I1 (see figure 2.7) generally document the beam path well enough and the beam path can be adjusted with the flipper mirror holder and one other mirror holder after iris I0. With respect to the irises I2 and I3, a finer adjustment is always possible. However, when enough input power is at hand and the beam path can be roughly approximated, it was found that this step doesn't play a crucial role in getting a good overlap signal.

- **Step 2: Get spatial overlap.**
  The two beams after the beamsplitter have to be spatially overlapped in their focused region at the NLM. It was found, that this is favourably done with the transmitted beam over mirror M_1. The focus of the transmitted beam has to be guided on top of the other focus, which tends to be very hard to quantify due to the mis-

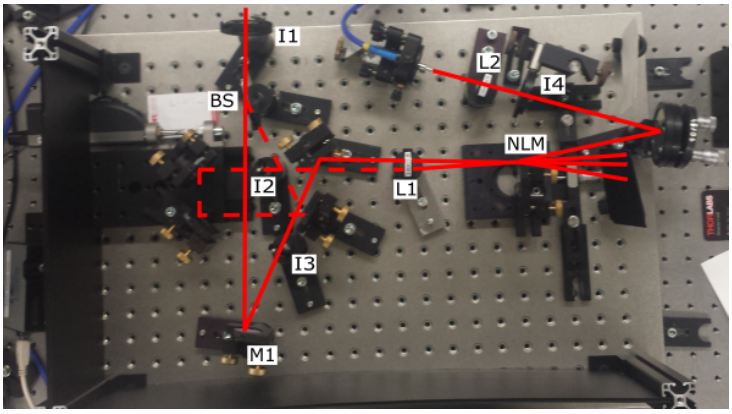

Figure 2.7: The SD-FROG apparatus in the laboratory.

match in intensity between the two beams. Moving the beam with M_1 shortly away and again backwards gives a good hint on the two positions.

- **Step 3: Get temporal overlap.**
  With the stage actuator (Newport CONEX-LTA-HS), a manual temporal scan be performed. For this it is very useful to know, at which position the overlap should be found, which should be documented every now and then when an overlap signal is stable (for the current setup, the overlap is approximately at 25.95 mm). With the matlab function *showStagePos*, the current position can always be read out. When a temporal overlap is found, two additional beams (the self diffracted ones) become visible after the NLM at the outer sides of the transmitted beams. They are preferably viewed on a white card. Due to the short pulse durations, these beams are often only visible for very short temporal distances. When no overlap is found, a higher input power can be tried, since the $\chi(3)$-signal is very intensity dependent. Furthermore, steps 1 and 2 may need to be repeated.

- **Step 4: Couple signal into glass fiber.**
  From the two visible diffraction points, both can be taken as the autocorrelation signal. However it was found, that for SHG light, the left point (seen from the NLM) has a higher intensity. Therefore, a mirror is set to reflect the diffracted beam to another (50 mm) lens, which focuses the autocorrelation signal into a glass fiber. In order to minimize SHG background signal in the spectrometer, an iris aperture is set before the lens, which should be completely aligned with the diffracted beam. Furthermore, stray light can be reduced with a dark beam block (black paper) beside the diffracted beam, that blocks the transmitted beams after the NLM. The glass fiber is mounted in a 5-axis mount (Thorlabs), which is used to optimize the autocorrelation signal once an overlap is visible in the spectrometer. This is the case, when the signal in the spectrometer vanishes as the temporal overlap is

reduced (with stage). It should be stated, that very high intensities of the beams can burn the produced grating into the NLM, that also at state positions away from the overlap the diffracted signal is visible. The intensity of the beam should then be reduced and the glass plate (NLM) moved a bit in the focal plane to set the overlap position to an undestroyed location.

- **Step 5: Optimize overlap signal.**
  Once the overlap signal found its way into the spectrometer, the spatial overlap can be improved once more (step 2). A good FROG trace will be measured, if the contrast between the overlap signal and the remaining stray light in the spectrometer (away from temporal overlap) is high. Another optimization cycle with respect to this contrast should be done. It was found, that especially the iris apertures I3 and I4 (see figure 2.6), as well as the spatial overlap and the glass fiber position play important roles.

- **Step 6: Take FROG trace.**
  A FROG trace is measured with the matlab routine *SD_Quag* (see appendix A.4 for handling). The zero time-delay point should be defined (can be read out again with *showStagePos*). It is important to define the limiting time-points wide enough before and after the maximum, so that the whole overlap signal can be scanned. During the measurement, the signal shouldn't saturate the CCD chip in the spectrometer, since this will of course cause false results for the pulse lengths.

- **Step 7: Perform retrieval algorithm.**
  The last step is the performance of the iterative retrieval algorithm, to get the real pulse form (E-field vs. time). The program generates a guess pulse-form and tries to reproduce the FROG trace iteratively. By comparison of the retrieved FROG trace and the actual one, it generates a FROG error, which can be taken as an indicator of the accuracy of the result. The current praxis was that a FROG error of about 0.02 (meaning 2% deviation) is acceptable. The error can be reduced with an as constant autocorrelation signal as possible (meaning low fluctuations), a high density of datapoints and a high grid size, which however also causes longer convergence times. In the laboratory, a separate program is used for the retrieval (for its usage compare with appendix 4). It also allows an image enhancement of the measured FROG trace via some background subtraction. A self programmed matlab function might be the better choice for the performance of the retrieval algorigthm, which would however require a deeper engagement to its mathematical basics. It is noted that at the homepage of Rick Trebino, matlab code can be downloaded as open source, however no option for the SD FROG method is implemented. Because the

retrieval algorithm differs only in some mathematical terms for the different FROG types (see ref. [9]), it should be not too hard to re-programme the existing matlab code.

2.4.3 Characterization of the SD FROG

Three examples for typical FROG traces, here in the case of the SHG of the femtosecond laser fundamental, can be seen in figure 2.8. The top images show FROG traces of chirped pulses, meaning that different parts of the frequency bandwidth of the pulse come at different times (have a different phase distribution). Therefore, the FROG trace has an oblique form, pending in opposite directions for negative and positive chirps. Since the direction of the time axis is arbitrary, the directions for negative and positive chirps have to be defined on additional information. The phase retrieval algorithm gives a positive chirp dependence of the phase for the upper right form in figure 2.8.

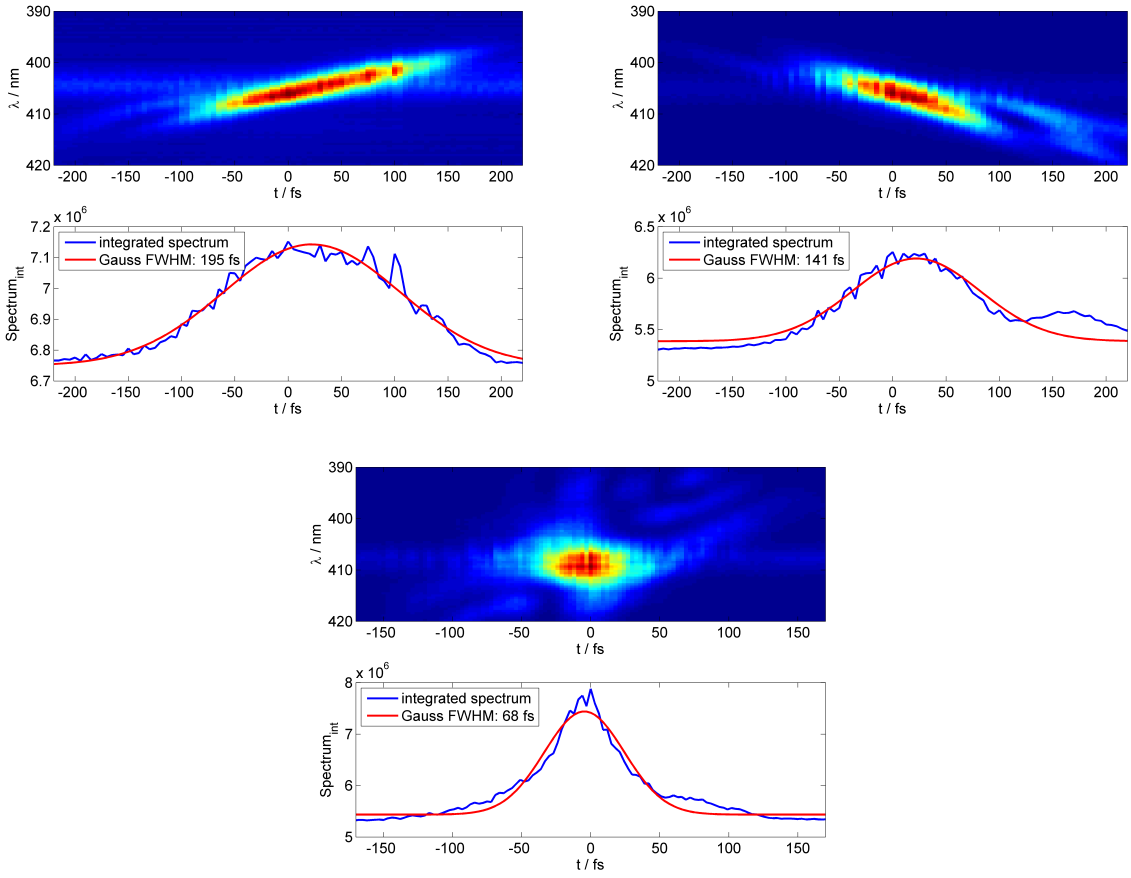

Figure 2.8: Three examples for FROG traces and their autocorrelation curves of the SHG for three typical cases: a negatively chirped pulse in the top left image, a positively chirped pulse in the top right image and an unchirped, short pulse in the bottom image.

The chirp direction was also checked with the introduction of a significant amount of glass before the FROG, which causes the generation of positive chirp due to normal dispersion in glass (Measurement date: 06.10.2016).

In order to verify the correct measurement of pulse durations (in the case of the FROG: for the correct retrieved pulse duration), a comparison was made with the 800 nm fundamental of the femtosecond laser. Because of the much higher intensity and broader pulse profile, a FROG measurement with the fundamental is much easier than with the second harmonic. However, the high intensities tend to easily destroy the non-linear medium. For the 800 nm wavelength, a single-shot-autocorrelator (SSA, company Coherent - described in more detail in ref. [12]) is available in the laboratory. This autocorrelator maps a spatial overlap signal to a temporal profile and can therefore be used to compare it with the retrieved FROG pulse duration. The results are shown in table 2.2. The pulse durations are comparable, with slightly higher pulse durations measured with the FROG, however the uncertainties of both methods are yet not fully clarified and are estimated to be in the range of the difference (Measurement date: 22.08.2016).

Table 2.2: Comparison of retrieved FROG pulse duration and SSA pulse duration

pulselength SSA / fs	**pulselength FROG / fs**
28	34
31	39

To quantify the accuracy of the FROG pulse duration, a series of measurements was performed to determine the statistical FROG uncertainty. Ten separate FROG traces were measured with the SHG, realigning the overlap on purpose in between. A standard deviation of about 5% was found, which was taken as uncertainty value for pulse duration measurements from there on, however systematic errors are still not excluded, since this uncertainty still doesn't explain the deviation in table 2.2 (Measurement date: 02.11.2016).

2.5 Temporal pulse shape modification

2.5.1 Principle

One of the single-pulse parameters that can be changed is the pulse duration and with it its spectral content distribution over time (chirp). The Coherent Legend laser amplification system used in the laboratory is a *chirped pulse amplifier*. The amplification in the amplifier-crystals happens with an artificially extended pulse duration, reducing the

intensity and therefore the risk of damaging the materials. Before the exit of the laser pulses, a grating compressor (see figure 2.2 and figure 2.9) is used to reduce the pulse duration and go to the limit of the transform limited pulse. However, a deviation from this shortest pulse length might me desirable in some cases:

- A generation of positive chirp in optical elements after the laser exit (e.g. in lenses, glass windows etc.) can be pre-compensated with an adjustment of the compressor such that the pulse at the exit has a negative chirp.
- Whenever measurements with a variable pulse length (e.g. PEPICO one pulse measurements - compare with chapter 3) are performed, the grating compressor allows a lengthening of the fundamental pulses in both chirp directions.

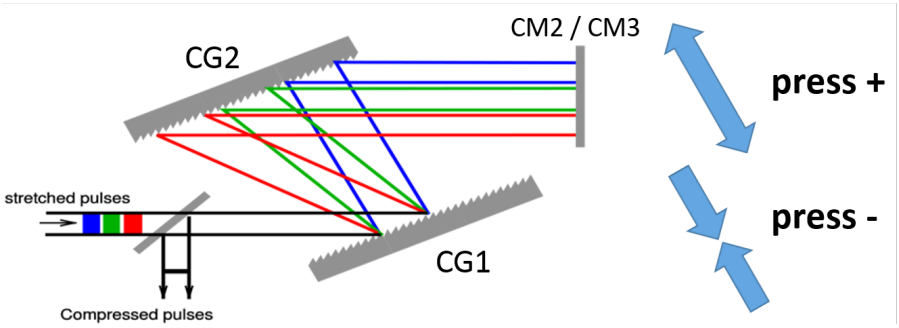

Figure 2.9: Schematic principle of the grating compressor: the stretched beam enters the compressor, gets diffracted at both gratings CG1 and CG2 and is then moved one level up with the mirrors CM2 and CM3, to hit the gratings one more time before leaving the compressor.

The compressor is aligned with two gratings (see figure 2.9), which mutual distance can be changed by an external controller. Pressing the '+' button increases the distance and therefore produces a negative chirp (the red part of the spectrum goes a longer way and is behind the blue part at the laser exit), pressing the '-' button the opposite. Unfortunately, no direct measurement of the compressor position is possible and the controlling is not discretized, but seems to work with an analogous signal. The pulse duration and form can be characterized with the FROG afterwards (section 2.4). The change in chirp with the compressor is however always linear and higher order chirp effects cannot be compensated.

It was found, that the effect of a change in the temporal pulse form of the femtosecond laser fundamental (800 nm) with the compressor had nearly the same effects also on the second harmonic. A fast way to get to the nearly shortest pulse duration is aligning the compressor to get a maximum conversion efficiency (high amount of 400 nm in the spectrum). The efficiency is highest when the fundamental beam is as short as possible (and has therefore the highest peak intensity).

2.5.2 Possible problem: non-parallel gratings

After a laser alignment in the Legend amplifier, a beamwalk appeared when changing the grating distance (trying to produce chirp). Somehow the gratings were not parallel anymore and therefore also the incident angle was changed when changing the distance. The solution was the following: align the incoming beam at first with a removable iris before the compressor (see manual). With the outer rotary knobs, change the angle of CG1, until the two beams on it are parallel. Then change both CG1 and CG2, that the outgoing beam is on the proper removable iris aperture. The cause for the problem was an induced stress on the gratings due to a tension on the adjustment cable (from CG2 to the outer rotary knob) when moving the gratings (Measurement date: 12.10.2016).

2.6 SHG energy determination

A problem with the measurement of frequency doubled output powers after second harmonic generation is that always parts of the laser fundamental propagate along with it. Therefore, a power measurement with a standard powermeter (in laboratory e.g. Coherent PowerMaxx) measures always the sum of both the energies of the fundamental and the second harmonic. A solution to this is the spatial separation dependent on the wavelength with a dispersive prism (see figure 2.10). Although a significant part of the output powers will be lost due to reflections on the prism surfaces, an idea for the correct ratio between the powers of the second harmonic and its fundamental can be deduced. Of course, the longer the distance between prism and power measurement point, the stronger is the separation.

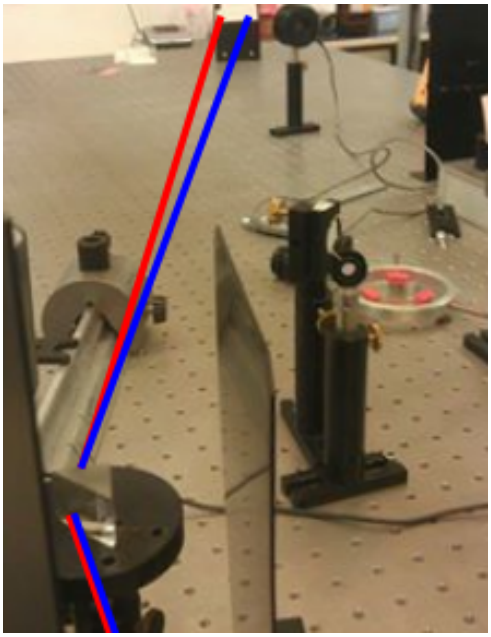

Figure 2.10: Spatial splitting of the two parts of the laser beam with a prism.

2.7 Optical Parametric Amplifier

During the working period of this master thesis, an Optical Parametric Amplifier (OPA) of type OPerA-Solo of the company Light Conversion (distributed by Coherent) was introduced to the laboratory and first measurements to deterimne performance and stability were performed. The main part of its functionality and the working principle with all

optical components can be found in the user's manual [19] and only its basic components and functions are explained here.

2.7.1 Basics

The OPA allows over various non-linear optical mixing processes the variation of the output pulse wavelengths between 240 and 2600 nm with an input pump-wavelength of 800 nm. The pump beam is split after the femtosecond laser output with a high-reflection beamsplitter (compare figure 2.2) and is guided over a mirror telescope into the OPA. A first beamsplitter (BS1, reflectivity: 98 %) separates the main part of the power for a second amplification stage, while the minor part is guided to the first amplification stage. At a second beamsplitter (BS2), the transmitted part is used for white-light generation in a sapphire crystal and is then non-collinearly, temporarily overlapped with the reflected part of BS2 of the pump beam in a first amplifier crystal (NC1). Over a time-delay stage one can change the part of the white light, which overlaps in time with the pump beam and can therefore scan the signal wavelength which is parametrically amplified in the crystal. The residual pump and idler beams are blocked and the signal beam is guided to a second amplifier crystal (NC2), in which it is again temporarily, and know collinearly, overlapped with the major part of the pump beam (reflected part of BS1). Signal and idler beams are formed, which have as sum always the frequency of the pump beam:

$$\omega_{signal} + \omega_{idler} = \omega_{pump}$$

Various non-linear optical mixing elements exist that allow the manipulation and conversion of the signal and the idler beam. For example, in the SH(SFS) mode, the second harmonic of the sum-frequency mixed signal of the signal beam with again the pump beam is amplified. Or in SH(SHI), the second harmonic of the second harmonic of the idler (so its fourth harmonic) is generated. For a proper separation of the generated wavelenghts from the fundamental and other residual wavelengths, different dichroic mirrors are on hand. A good summary of all the different wavelength ranges and which optical components have to be used can be found in the OPerAs manual [19].

2.7.2 Stability of the OPA output signal

A major requirement for performing, for example, pump-probe measurements with the OPA in future will be an as constant output signal as possible, meaning low fluctuations of the pulse-to-pulse energy. The output power and its noise are at best characterized with the Coherent EnergyMax sensor (J-10MT-10KHZ). It is a pyroelectric sensor and has therefore a very high temporal resolution and allows a statistical evaluation of the

pulse-to-pulse fluctuations. Attention should be paid to the maximum allowed average power of 1 W on the sensor. It was noticed, that for every amplification range, the most stable (and also the highest) output power can be achieved in the middle of the calibration curve, for example in the SHS mode (580-800 nm) with approximately 690 nm. Especially at the edges of the curves, the output stability and output powers are significantly lower. As a general rule of thumb, it can be said that a high output power comes also with a good output stability.

There are several adjustments that can be done in the OPA, that allow a maximization of output powers. It is presumed, that the major components of the OPA have been aligned properly. The WLG should be clearly visible and a low amount of superluminescense should be seen at the point of beam block for the residual pump beam after NC1 (the best visibility of superluminescense is achieved with 1600 nm signal).

- **Incoupling of pump beam:** The beam path before the OPA is well documented with three iris apertures before and after the telescope. When the beam is aligned to them, it was found that the best way to further align the beam is to move the beam onto the removable aperture before NC2 with the last mirror before the OPA entrance (see manual, ref. [19]). If amplified output power is detected, the incoupling can be also optimized with the last mirror before the entrance with respect to the output signal.
- **White light generation (WLG):** In order to check correct WLG, the second stage pump beam should be blocked for safety reasons. A small white paper stripe can be placed before L4 (see manual) and the amount of white light can be adjusted with the aperture A2. It was noticed, that the best and stable output powers could be achieved with a high amount of white light intensity, even slightly higher than saturation, so that the white light rainbow pattern even becomes unstable. However, for a proper optimization, again the WLG can be adjusted with respect to output power.
- **Change chirp:** Because various optical elements that produce first and also higher order chirps are present in the OPA, is it recommended to always optimize the chirp with the grating compressor to optimize the OPA output power. However, one always has to keep in mind, that a chirp modification has an influence on the generation of white light and therefore the WLG might has to be modified again afterwards.
- **Delay 2:** This delay optimizes the temporal overlap between the 98 % part of the pump beam and the signal in the NC2. It should be optimized every now and then

to get a maximum OPA output power. This can be done with the WinTOPAS software tool provided by the manufacturer via *Curves* and *Offsets*. Here the offsets for all motors can be optimized and changed and saved to the whole calibration curves for all wavelengths.

It was found, that a closed cover of the OPA somehow slightly changes the beam path in the amplifier (maybe inducing some internal stress or because of fluctuations due to air turbulences). A fully optimized OPA with open cover is not in its optimal configuration (with respect to output power) when the cover is closed. Because of this and because the overall stability of the OPA output is much better with a closed cover, all the optimization parameters should be optimized keeping it closed, which is however not possible for the WLG. Also, the beam path before the OPA (after laser exit, beamsplitter and telescope) was enclosed completely in order to minimize air-influences.

OPA optimization procedure

Because the WLG and chirp both play a crucial role in producing high output powers, their lone optimization might not produce the best output signal. In order to get to the real global maximum, the following optimization routine is recommended:

- check WLG -> optimize with aperture A2
- check chirp -> optimize for best WLG
- check superluminescense of the residual pump beam after NC1 with 1600 nm
- check SHG of signal after NC1 with 1300 nm (orange beam)
- check output power with 1300 nm
- optimize incoupling (mirror before entrance), chirp and WLG for maximum output power
- optimize delay 2 for temporal overlap in NC2
- change chirp away from optimum ('+' or '-')
- change WLG back to maximum output power
  => output signal higher than before last step?
  yes: => repeat last step in same chirp direction
  no: => change chirp and WLG back and try other chirp direction
- find global maximum with the last two steps

2.7.3 Reducing OPA output power

In order to be able to control the amount of ionization from OPA laser beams in the measurement chamber, the output power, which is in general much too high, should be reducible in a controllable manner. Several methods were tried: The introduction of an

ultrathin Pellicle beamsplitter (the same as used in the FROG autocorrelator, see 2.4) turned out to be not successful due to a damaging of the beamsplitter due to the high output powers. A better reduction could be achieved with a 1 mm fused silica glass plate (Thorlabs), where a power reduction of about 50 % could be reached (Measurement date: 2.11.2016).

It was also tested to reduce the output power with a change of the *Delay 2*, reducing the temporal overlap in the NC2, however a power reduction also caused a strong increase of fluctuations due to a loss in saturated amplification (Measurement date: 28.11.2016). A good way to reduce intensity in the laser focus in general could also be the introduction of a mirror telescope after the OPA exit to introduce a divergence and widen the beam diameter in the overlap region with the probe focus inside the measurement chamber.

2.7.4 Common problems

No output power measured => reset all motors:
Before trying to optimize all other parameters, a reset of all the servo-motors with the WinTOPAS software should be tried. The software links the true position of the motors with a calibrated position of a tuning curve. If the OPA wasn't turned on for a long time, the zero-point position can be related to the actual position and the calibration completely fails. In order to reset, go in the WinTOPAS software to *Motors* and *Direct access* and press *Reset all*. The motors move to their mechanical zero position and save this value to the lowest value in their calibration curve.

2.8 PEPICO spectra shape analysis and possible problems

During the working period, several problems regarding the width and the shape of the PEPICO spectra occurred. Regarding many of the problems it can be stated in conclusion, that a complete bake-out process should be performed every now and then to get rid of possible contaminations.

2.8.1 Electron spectra shape distortions

A problem with a very broad electron spectrum appeared. The signal to noise ratio was nearly catastrophic and no clear electron peaks at all could be identified (see figure 2.11, left). Several SHG adjustments were tried to fix the problem, including varying the wavelength, changing the crystal and varying the chirp (at this moment the influence of

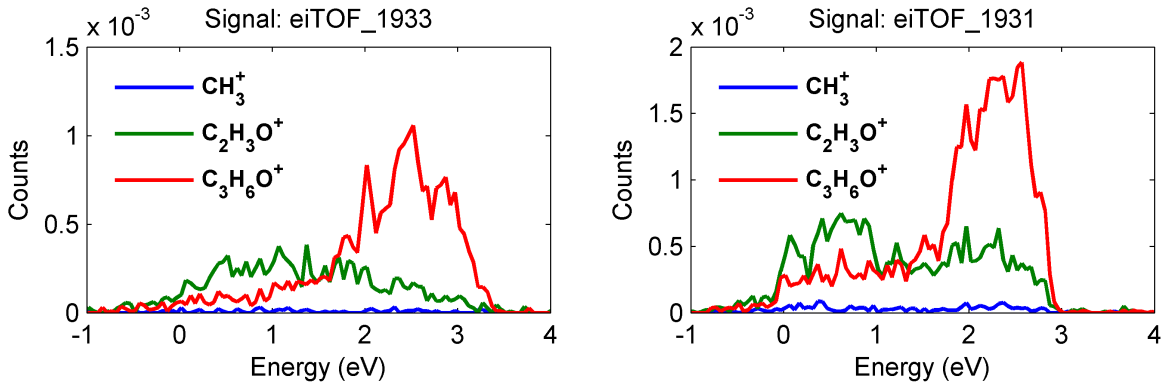

Figure 2.11: False and correct PEPICO spectra shape, evaluated with Covariance. Left image: repeller z-position -7 mm, right image: repeller z-position -11 mm

all these factors on the spectra wasn't as well understood as at the end of the working period). It was found, that the crucial factor was the z-position of the repeller electrode in the time-of-flight spectrometer, which turned out to be much too close to the laser focus. Before the problem occured there had been several adjustments on the beam paths (changing to non-collinear setup, described in ref. [15]). A major part of stray light hit the repeller and caused the strange spectra shape. The repeller position was changed from -7 mm to -11 mm (2 mm from the position of stray light from the repeller) and the spectra looked normal again (see figure 2.11, right). A hint to a repeller problem could have also been the performance of 'FileDiagnostics.m' (see appendix B.2), which is nowadays standardly performed after each measurement. The FileDiagnostics for the measurements seen in figure 2.11 indicate, that the ratio between the detected electrons and ions for the file *eiTOF_1933* (left image) is approximately 0.5, which hints directly to a false detection and therefore a false repeller position. The ratio should always be higher than 1, because electrons are detected more efficiently than ions [14]. For example in *eiTOF_1931* (right image) the ratio is 1.36 (Measurement date: 29.05.2016).

2.8.2 Reduction of MCP peak heights

The problem described in this section and also the one in section 2.8.3 appeared after a significant moving process of the measurement chamber out of the laboratory rooms. Due to problems with the illumination system a service visit had to be performed and the measurement chamber with the TOF-spectrometer was moved to the neighboring rooms. During the moving process, the turbo pumps were shut down and therefore only raw vacuum conditions (>1e-3 mbar) were achieved.

After moving the measurement chamber back into the laboratory, the first measurements showed a significantly reduced electron and ion signal that could be measured. After an

inspection of the time traces (compare with section 2.2) it was found, that the peak heights of the electron and ion hits had been significantly reduced and therefore a great part of the hits couldn't be detected with even very low discriminator levels. The comparison between mean peak heights gave now about 45 mV peaks vs 280 mV peaks before. The speculation was, that somehow during the movement process described above, the Multi Channel Plate (MCP) detector was influenced (material deposition etc.) and therefore its voltage pulses were not as high as before. After an increase of the MCP voltages from 2.09 kV to 2.30 kV (MCP back) and 2.5 kV to 2.8 kV (phosphor screen) the same peak heights and signal counts could be detected as before. However, after a bake-out process that was performed some weeks later, the MCP was suddenly in saturation (peak heights > 1V) and therefore the MCP voltages could be reduced to their previous values. In conclusion, whatever change may have caused the drop in signal from the MCP, the problem could be reversed by the baking process (Measurement date: 18.08.2016).

2.8.3 Strong electron background signal

While performing a long enduring pump-probe PEPICO timescan it was found, that a high electron signal was added to the PEPICO spectra at lower kinetic electron energies (see figure 2.12). This part increased over the measurement day, which could also be seen by an obversation of a constant rise in electron counts (*FileDiagnostics*). By reducing the vapor pressure (<1e-8 mbar) it was found, that the signal was not due to the gaseous species that was measured at that time (acetone), but rather due to some background gas that got somehow into the chamber. It was found, that when turning off the solenoid current (3 A, magnetic bottle [14]), the background signal vanished after about a day pumping the chamber. The solenoid heats up when it is turned on for longer times, which is the case during time-consuming pump-probe PEPICO measurements. There seemed to be some material on the solenoid which got desorbed due to the heating process.

The solution was a complete bake-out of the measurement chamber, including heating up the solenoid to about 100°C. Attention should be paid that the temperature around the solenoid doesn't exceed about 150°C due to the surrounding magnetic material (μ-metal). The background signal nearly vanished after two days baking out the chamber (Bake-out starting date: 07.09.206). In order to avoid possible influences, the solenoid should be turned off always when not needed to let it cool down. This was also practiced while performing a long term timescan, the solenoid was turned off for about 10 minutes between every three or four time-steps. This led of course to quite long measurement times for the complete timescan of approximately 13 hours.

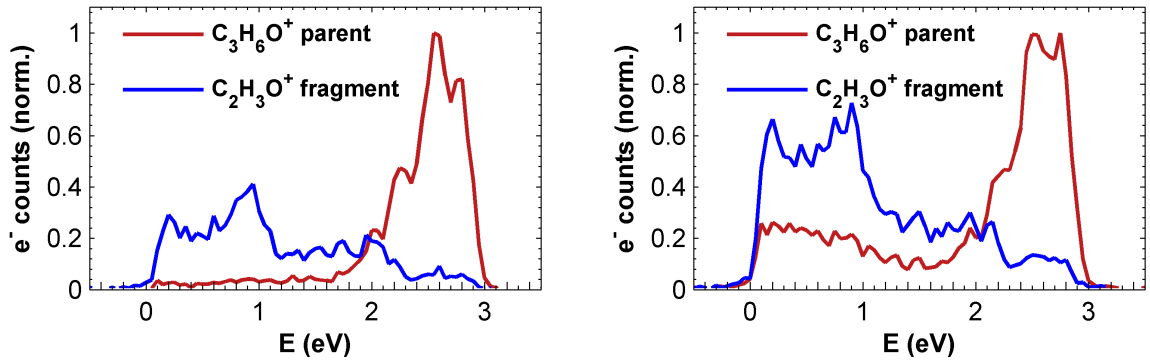

Figure 2.12: Demonstration of a change in the PEPICO spectra of two pump only measurements, one at the beginning (left) and one at the end (right) of a tried timescan. The higher signals at low energies are due to a high electron background, which causes false coincidences.

2.8.4 Electron spectra shift

Once various measurements, especially when performing long timescans, showed a continuous spectra shift of the electron spectra to higher or lower energies (often several eV between two measurements). This was especially tedious when performing PEPICO timescans, because all taken spectra had to be shifted manually to their zero-energy position (variable *enplotoff* in PlotCov_BG, see appendix B.4), which also introduced a systematic error, especially when subtracting two spectra (pump-probe minus pump-only) that were shifted differently. At some point, the spectra drift stopped or became negligible, such that the manual shifting would have introduced a bigger error. No major spectra shift could be observed any more (Test measurements: 16.06.2016, 24.06.2016). In conclusion, the cause for the shift is not known, as possible reasons, a charging of the repeller (causing a non-constant potential) or a non-perfect grounding of the flight tube were discussed. A reason for a stop in spectra movement may have been a new adjustment of the laser focus position with respect to the repeller, maybe indicating the first of the two discussed causes. When a spectral movement should be observed again in future, also a voltage measurement of the repeller voltage is recommended, in order to exclude possible influences of the voltage source.

CHAPTER 3

Results

3.1 Ultrafast photofragmentation dynacmis in acetone

The main part of the following chapter was submitted in a peer-reviewed journal with the title "Direct observation of a photochemical activation energy: A case study of acetone photodissociation". Additional remarks were added here in order to give more detailed explanations. In the following table, the contributions of the authors to the different development phases of the article are listed:

contribution	**authors**
funding:	Wolfgang E. Ernst, Markus Koch
design of the experiment:	Markus Koch
preparation / setup:	Bernhard Thaler, Pascal Heim
data acquisition:	Bernhard Thaler, Pascal Heim, Markus Koch, Markus Kitzler
data analysis:	Bernhard Thaler, Pascal Heim
interpretation:	Markus Koch, contribution: Bernhard Thaler, Pascal Heim
publication writing:	Markus Koch
proof reading:	Markus Koch, Pascal Heim, Bernhard Thaler, Markus Kitzler, Wolfgang E. Ernst
additional:	FROG setup (1st version): Markus Kitzler

3.1.1 Introduction

Acetone, chemically more accurately known as 2-propanone, is the simplest ketone, consisting of an oxygen atom doubly bound to a carbon atom and two additional methyl-

groups sitting around the carbon. The photodissociation of acetone has been widely studied (ref. [20]) and also been investigated by our group with time resolved pump-probe experiments with an excitation wavelength of 266 nm and an ionization pulse of 400 nm [8]. The most common photofragmentation process is the formation of an acetyl (C_2H_3O) and a methyl (CH_3) radical, as is depicted in figure 3.1.

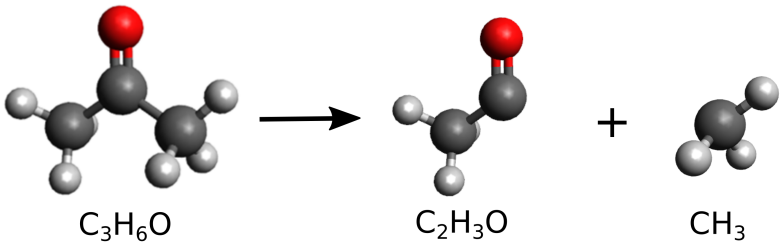

Figure 3.1: The most common photofragmentation reaction of acetone: the parent molecule (often already as ion) dissociates into an acetyl and a methyl radical.

Photoinduced fragmentation of molecules can be caused by different mechanisms. For example, ionization to different cationic states yields different ion fragments because different electrons (HOMO, HOMO-1, ...) are taken from the molecule [6], [7]. If excited states of the neutral molecule are involved in the ionization process, internal conversion (IC) can occur and strongly influence which cationic states are accessed [7], [21]. IC is accompanied by nonadiabatic coupling of electronic and nuclear degrees of freedom and thereby facilitates the conversion of electronic to vibrational energy. In this case, even ionization to the ionic ground state can lead to fragmentation because energy is coupled into vibrational modes of the molecule. This vibrational energy is first concentrated in one or few modes and will subsequently be distributed to other modes by intramolecular vibrational energy redistribution, causing the breakage of chemical bonds. Photoinduced fragmentation of acetone is one of the most comprehensively studied photochemical reactions [20]. The highest occupied molecular orbital (HOMO) of acetone can primarily be described as lone pair at the oxygen atom with non-bonding character [22]. The molecular geometry is therefore not changed by photoexcitation to Rydberg states or even by photoionization of the HOMO electron [23]. The energies of the ns, np and nd Rydberg series have been accurately determined in synchrotron experiments [24], [25]. These Rydberg states are crossed by valence states, which provide efficient relaxation pathways [23], [26]. Excitation to high-lying Rydberg states shows ultrafast population transfer to lower-lying Rydberg states [8], [27]. After excitation to the energy range of 9.2 eV, corresponding to population of the 5p, 5d, 6s, 6p, 6d, 7s states, IC to the oxygen 3p Rydberg states was observed as one of the relaxation channels [8]. This channel facilitates fragmentation to acetyl ions and methyl radicals, with the fragmentation process happening after the ion-

izing probe pulse, as was clearly shown by photoelectron-photoion coincidence (PEPICO) detection.

In this work we apply a resonance-enhanced four photon ionization scheme (three-photon excitation and one-photon ionization) at 3.1 eV photon energy with pulse durations in the range of the characteristic time of the IC process. With this scheme we are able to observe the state specific fragment-to-parent ratios not only of the 3p state as previously [8], but of several lower Rydberg states populated by IC. This allows us to directly determine the activation energy for fragmentation, a quantity of central importance to photofragmentation. Variation of the pulse length in the range of 100-200 fs with positive and negative chirps allows us to investigate and influence the fragmentation behavior. By varying the photon energy we scan the excitation energy across several members of the ns, np and nd Rydberg series and observe the dependence of the fragmentation process on the excitation energy. PEPICO detection allows to distinguish different ionization channels and to observe the dynamics and fragmentation behavior of each channel [8]. The photoelectron (PE) kinetic energy provides information about the chemical composition and excited state of the molecule at the instant of ionization. It can clearly be distinguished whether fragmentation occurs in the neutral before ionization or in the ion after ionization. Correlation with ion masses for each ionization event allows to determine the threshold energy for conversion from electronic to vibrational degrees of freedom, in order to facilitate fragmentation, thereby also providing an insight into the redistribution of vibrational energy.

3.1.2 Peak assignment

Ionization of acetone molecules with laser pulses of 3.1 eV photon energy (approx. 400 nm wavelength) and 100-200 fs pulse duration results almost exclusively in the formation of unfragmented acetone parent ions ($C_3H_6O^+$, 58 amu) and acetyl fragment ions ($C_2H_3O^+$, 43 amu). Figure 3.2 shows photoelectron spectra recorded in coincidence with parent ions (red line) and in coincidence with acetyl fragment ions (blue line). Both the parent and fragment PEPICO spectra consist of several peaks, which can be assigned to one-photon ionization from different Rydberg states. These are populated either directly by three-photon excitation from the ground state, or by IC to lower Rydberg states, as indicated in fig. 3.3. IC can proceed directly between Rydberg states that are close in energy [28], or via valence states that cross and provide efficient relaxation pathways [23], [26] (orange dotted arrow in fig. 3.3). We note that the shape of the spectra cannot be explained with ionization originating from one Rydberg state and leading to vibrational excitations in the ion, because the most dominant vibrational modes activated by photoexcitation are

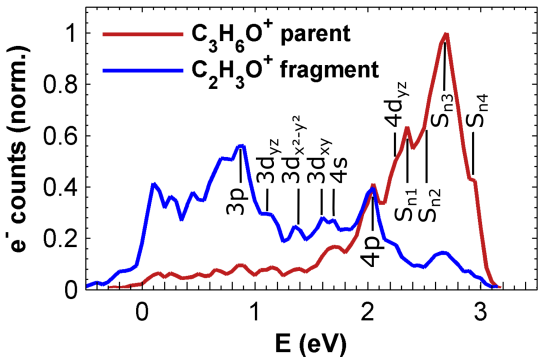

Figure 3.2: Acetone parent PEPICO (red) and acetyl fragment PEPICO (blue) spectra obtained with resonant three-photon excitation and one-photon ionization with 3.14 eV photon energy. Assignments to Rydberg states are indicated, as listed in tab. 1. The pulse length was 75 fs and the spectral fwhm of the pulse was 33 meV.

too low in energy (the CCC deformation ν_8 and CO in-plane bending $\nu_1 9$ with respective excitation energies of only 39 and 51 meV) [24].

Tab. 3.1 lists the observed PEPICO peak positions $E_{e,kin}$ together with the level assignments and deviations (E_n-$E_{n,lit}$) to line positions obtained from high precision synchrotron experiments [24], [25]. For electron energies up to $E_{e,kin}$ = 2.25 eV a single Rydberg state can be assigned to each PE peak (with exception of the closely spaced $3p_x$, $3p_y$, $3p_z$ and $4p_y$, $4p_z$ states). Above $E_{e,kin}$ = 2.35 eV, where the energetic distance of states drops below the three-photon bandwidth, we group the np, nd, and (n+1)s states to obtain a Rydberg series, each member of which is assigned to one PE peak. For simplicity, we label these groups S_{n1}, S_{n2}, S_{n3}, and S_{n4} (tab. 3.1). Some states, which are represented as a weak shoulder and are barely visible in fig. 3.2, can be better identified in figs. 3.4 and 3.5. The proposed assignment agrees very well with the line positions documented in literature and the deviation (E_n-$E_{n,lit}$) of the observed PEPICO peak positions is with one exception less than the experimental resolution of 150 meV (spectrometer resolution and laser bandwidth). We note that the np_x (n>3), nd_{z^2}, nd_{xz} states are not included in our assignment because no exact state energies are available, as their excitation is symmetry forbidden with single photon excitation from the ground state [24], [25].

Three-photon excitation with 3.14 eV photon energy provides a total excitation energy of 9.42 eV. Considering the 33 meV fwhm spectral bandwidth, the S_{n4} (7p, 7d, 8s) and S_{n3} (6p, 6d, 7s) states can be excited (tab. 3.1, fig. 3.2), which are represented by the parent PEPICO peaks at 2.95 and 2.70 eV, respectively. The parent and fragment PEPICO spectra in fig.3.2 clearly show PE peaks below 2.70 eV, which we assign to the members of the ns, np and nd Rydberg series, as listed in tab. 3.1. Above 2 eV the PE peaks are detected mainly in coincidence with parent ions, while below 2 eV the

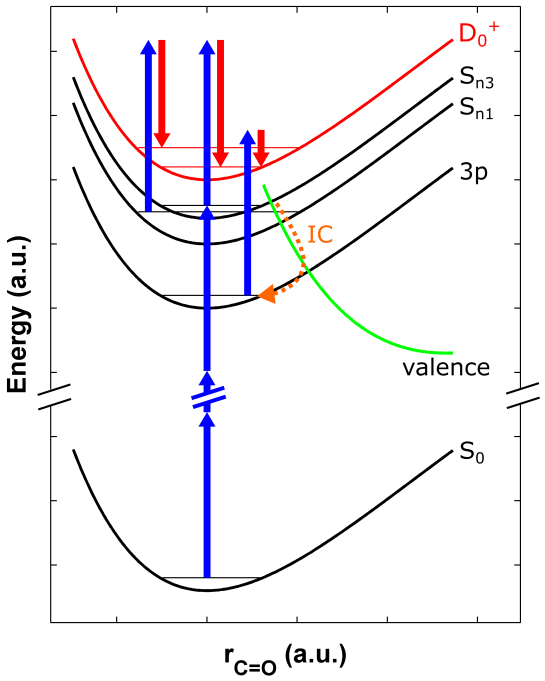

Figure 3.3: Schematics of selected potential energy curves along the C-O bond-stretching coordinate to visualize assigned ionization and electronic relaxation channels. The shapes and distances of the potential energy curves are not to scale and only three Rydberg states are selected from the dense region above the 3p states (c.f. tab. 3.1). Three-photon excitation (blue upward arrows) from the S_0 ground state directly excites the S_{n3} states. Lower Rydberg states (S_{n1}, 3p) are populated by IC, either directly due to vibronic coupling, or mediated (orange dotted arrow) by crossing valence states (green). Ionization of each Rydberg state by a fourth photon proceeds to the corresponding vibrational level of the ionic ground state (D_0^+, red curve), because the Rydberg states share the same geometry as the ionic ground state. The PE kinetic energies (red downward arrows) thus reflect the vertical ionization energies of individual Rydberg states.

fragment PEPICO signal dominates. This important fact provides information about the fragmentation behavior and will be considered below. Beforehand, it is important to discuss the mechanisms leading to population of these lower Rydberg states. Since the HOMO electron has nonbonding character, the molecular symmetry of the ground state is very similar to that of the corresponding Rydberg states, as well as to the symmetry of the lowest ionic state. Therefore, the potential energy surfaces of these states appear to be parallel [23] and vibronic 0-0 transitions are dominant [28], as indicated in fig. 3.3. The laser bandwidth is too narrow to excite 0-0 transitions to Rydberg states below S_{n3}. States below 9.27 eV (S_{n3}) are thus populated by electronic relaxation through IC [23],

Table 3.1: Peak positions of the PEPICO spectra shown in fig. 3.2 (photon energy hν = 3.14 eV). $E_{e,kin}$ ... electron kinetic energy; E_n ... calculated Rydberg state energy, $E_n = IE - (h\nu - E_{e,kin})$, IE = 9.708 eV [24]; $E_{n,lit}$ ... literature values of Rydberg state energies [24]. Energies $E_{n,lit}$ of the groups S_{n1}- S_{n4} are averaged over the individual states.

$E_{e,kin}$ / eV	E_n / eV	assignment	$E_{n,lit}$	E_n-$E_{n,lit}$
2.95	9.52	S_{n4} (7p, 7d, 8s)	9.41	0.11
2.70	9.27	S_{n3} (6p, 6d, 7S)	9.30	-0.03
2.55	9.12	S_{n2} (6p, 6d, 7S)	9.10	0.02
2.35	8.92	S_{n1} (6p, 6d, 7S)	8.83	0.09
2.25	8.78	$4d_{xy}$	8.70	0.08
2.05	8.62	$4p_y$, $4p_z$	8.58	0.04
1.70	8.27	4s	8.22	0.05
1.60	8.17	$3d_{xy}$	8.17	0.00
1.35	7.92	$3d_{x^2-y^2}$	8.09	-0.17
1.15	7.72	$3d_{yz}$	7.72	0.00
0.90	7.47	$3p_x$, $3p_y$, $3p_z$	7.40	0.07
0.70	7.27	prob. valence		
0.45	7.02	prob. valence		
0.25	6.82	prob. valence		
0.10	6.67	prob. valence		

[26], [28] (orange arrow in fig. 3.3). Because IC can be a very fast process on sub-10 fs time scales [29], relaxation to and ionization from lower Rydberg states will proceed within the same laser pulse if the pulse duration is on the order of or longer as the IC time constant. IC populates different vibrationally excited lower Rydberg states, each of which is ionized to the corresponding vibrationally excited state of the ionic ground state, because the potential energy surfaces are parallel. This is indicated in fig. 3.3. For example, the photo-excited S_{n3} states in low vibrational levels are ionized to the same low vibrational levels of the ion, while IC to S_{n1} results in energy conversion to vibrations and consequently to ionization to vibrationally higher excited ionic states. The energetic distance of the respective Rydberg state to the ionic state, the ionization energy (IE), is obtained from the observed PE kinetic energy. The lower in energy the observed PE peak is, the more energy is deposited in the molecule and converted to vibrations. Ionization of states above 4p (2.05 eV) leads primarily to unfragmented parent ions, while ionization of states below 4p is dominated by fragmentation. It is important to realize that fragment PEPICO peaks are observed at PE energies that correspond to ionization from Rydberg states of the unfragmented acetone molecule. In fact, all fragment PEPICO peaks are also recognizable in the parent PEPICO signal. The electron kinetic energy, as observed in the spectrum, is determined by the chemical nature of the molecule at the

instant of ionization. Assignment of the acetyl fragment PEPICO peaks to excited states of the unfragmented acetone proves that the fragmentation process has not happened at the moment of ionization, but occurs in the ionic ground state after ionization. The fragment PEPICO peak at 0.90 eV is assigned to the states $3p_x$, $3p_y$, $3p_z$, which lie within 100 meV [24], [28]. The 3p states have been observed in previous experiments, further supporting our assignment [8], [27]. Because the next lower state to 3p, the 3s state at 6.37 eV [24], is too low in energy to be ionized with one photon, the PEPICO peaks below 0.90 eV could be, in part, related to a Norrish Type I dissociation of the neutral molecule with subsequent ionization of the acetyl radical [8]. Alternatively, a relation to valence states is possible: An avoided crossing of the $3p_y$ with the valence (π -> π^*) state leads to a double minimum potential [30], and thus to increased Franck-Condon overlap with higher vibrational states of the ion, which in turn yield a lower electron kinetic energy. The superior signal-to-noise ratio obtained with the resonance-enhanced four-photon ionization scheme of this work allows us to observe the weaker PE peaks above 3p, which was not possible in previous experiments [8]. The good contrast for these closely spaced PE peaks between 1 and 2 eV enables us to scan the excitation wavelength and observe the shift of the fragment-to-parent crossover, in order to obtain a deeper insight into the fragmentation dynamics and to determine the threshold energy required for fragmentation more precisely.

3.1.3 Wavelength variation

PEPICO detection clearly shows whether ionization from a certain excited state leads to fragmentation or not. For states that are populated by IC the amount of energy that is converted into vibrational energy (ΔE_{vib}) can be determined from the photon energy and the electron kinetic energy. In order to determine ΔE_{vib} we record PEPICO spectra for different photon energies, as shown in fig. 3.4. Most obvious, the parent PEPICO spectrum (fig. 3.4a) shows a strong dependence on the photon energy, while the fragment spectrum (fig. 3.4b) shows minor but never the less very important changes in the range of 1.5-2.5 eV. We first discuss the parent spectra before we determine ΔE_{vib} from the fragment spectra.

The parent PEPICO spectra for different photon energies are dominated by four structures at 2.05, 2.25-2.35, 2.55-2.70, and 2.95 eV, representing the 4p, $4d_{yz}$ /S_{n1}, S_{n2}/ S_{n3}, and S_{n4} states (tab. 3.1), respectively (note that $4d_{yz}$/S_{n1} and S_{n2}/ S_{n3} are close in energy). The total three-photon excitation energy is increased by 0.5 eV from 8.97 eV to 9.54 eV, which is represented by the shift of the high-energy edge of the parent PEPICO spectrum. The stepwise photon energy increase enables the excitation to successively higher Rydberg states. For example, with 8.97 eV excitation energy (photon energy hν

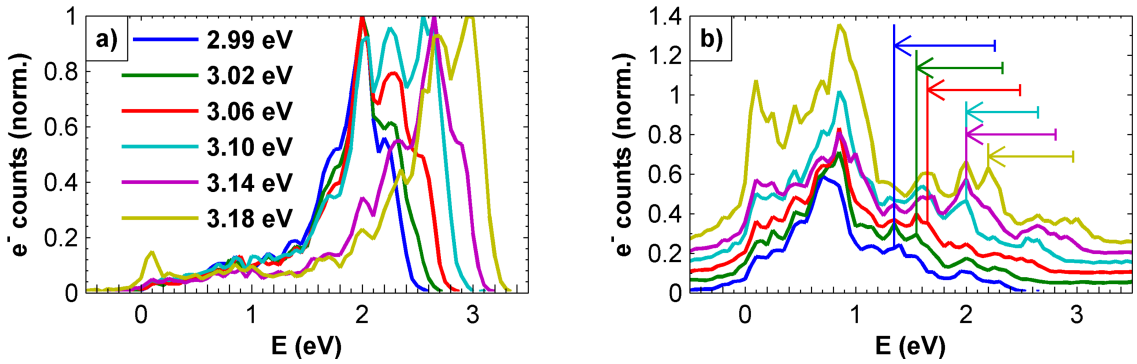

Figure 3.4: Acetone parent PEPICO (a) and fragment PEPICO (b) spectra obtained with different photon energies, as given in the legend. As in fig. 3.2, ionization is achieved by a resonant 3+1 photon transition. The pulse length was 150 fs (positive chirp) and the spectral bandwidth varied between 33 and 44 meV. The fragment and parent spectra at each photon energy are normalized to the highest parent signal. For clarity, the fragment spectra (b) are vertically offset by 0.05. Vertical lines indicate the highest-energy IC fragment peak (cf. tab. 3.2) and horizontal arrows indicate the amount of energy that is converted into vibrations during the IC process.

= 2.99 eV) the 4p states at 8.58 eV are excited and appear as dominant peak at 2.05 eV in the parent spectrum (blue line in fig. 3.4a). Increasing the excitation energy to 9.30 eV (hν = 3.10 eV, cyan curve in fig. 3.4a) results in additional ionization from $4d_{yz}$ /S_{n1} and S_{n2}/ Sn_{n3}. The highest excitation energy, 9.54 eV (hν = 3.18 eV, yellow curve), facilitates excitation to S_{n4}, with the strongest spectral feature at 2.95 eV. This spectrum additionally has contributions from all lower Rydberg members down to 4s, with decreasing amplitude. Considering the laser bandwidth as above, these states are populated by electronic relaxation (IC) between the S_{n4} states and the Rydberg states below, as will be discussed in more detail below.

Table 3.2: Photon energies and energy considerations for the PEPICO spectra in fig. 3.4. $h\nu$ ... photon energy; E_{max} ... position of the highest-energy IC fragment peak in the PEPICO spectrum (fig. 3.4b); state ... Rydberg state corresponding to E_{max}; $\Delta E_{vib} = 4 \cdot h\nu - (IE + E_{e,kin})$... energy deposited in the molecule.

hν / eV	3 $\cdot h\nu$ / eV	E_{max} / eV	state	ΔE_{vib} / eV
2.99	8.97	1.35	$3d_{x^2-y^2}$	0.91
3.02	9.06	1.60	$3d_{xy}$	0.78
3.06	9.18	1.70	4s	0.84
3.10	9.30	2.05	4p	0.65
3.14	9.42	2.05	4p	0.81
3.18	9.54	2.25	$4d_{yz}$	0.77

The photon energy dependence of the fragment PEPICO spectrum (fig. 3.4b) is different from that of the parent. While on the low energy side the positions of all PEPICO peaks remain constant, on the high energy side peaks appear that correspond to increasingly higher states for increasing excitation energies. As clearly seen in fig. 3.2, the fragment PEPICO spectra show relatively large peaks up to a certain energy limit (2 eV) and significantly smaller peaks above. The one of the larger peaks with the highest energy is important for us, as it represents the energy conversion threshold for fragmentation during the IC process. The smaller peaks, in contrast, are caused by a different fragmentation mechanism as we will show by pulse energy dependence measurements below. In fig. 3.4b, long vertical lines indicate the position of the highest-energy IC fragment peak for different excitation energies, and tab. 3.2 lists the corresponding energies (E_{max}) and state assignments. The amount of energy (ΔE_{vib}) that is converted into vibrational energy during the IC process can be calculated as difference between the energy of the four photons required for ionization and the IE plus the measured electron kinetic energy: $\Delta E_{vib} = 4 \cdot h\nu - (IE + E_{e,kin})$. The lower limit of ΔE_{vib} required for fragmentation is thus obtained from the highest-energy IC fragment peak in the PEPICO spectrum (tab. 3.2) and is indicated by the lengths of horizontal arrows in fig. 3.4b. For example, for $h\nu$ = 2.99 eV (blue curve in fig. 3.4b) we identify the highest IC fragment peak at 1.35 eV, meaning that IC to $3d_{x^2-y^2}$ yields fragmentation and ΔE_{vib} is determined to be 0.91 eV. The average of ΔE_{vib} over the six measurements with different photon energies is (0.79 ± 0.04) eV, which we take as the activation energy for fragmentation. As a side note we mention that the highest excitation energy of 9.54 eV ($h\nu$ = 3.18 eV) results in two peaks at very low kinetic energies emerging in both the parent and fragment PEPICO spectra (fig. 3.4). The parent and fragment peaks are of different origin as becomes clear from the spectra for even higher excitation energies of 9.67 eV (not shown). The parent peak at 0.1 eV is due to direct ionization with three photons, because the energy of three photons including the bandwidth is sufficient to reach the ionization potential of 9.708 eV [24]. Consequently, this peak grows significantly in the 9.67 eV spectrum. The fragment PEPICO signal, in contrast, shows a double peak structure and increases much less at 9.67 eV. We assign this peak to another relaxation-fragmentation channel that involves fragmentation of the neutral acetone molecule to an acetyl and methyl fragment in combination with subsequent ionization of the acetyl [8]. This channel seems to be weakly present for lower excitation energies and increases strongly for higher energies.

3.1.4 Pulse length variation

The results up to now have shown that IC leads to population of states that are energetically below the states in the excitation window. Depopulation of the Rydberg states in

this energy range was assigned with a time constant of (147 ± 28) fs [8]. Variation of the pulse duration in the range of 100-200 fs should therefore influence the PEPICO spectra. While the alteration is minor for the parent spectrum (fig. 3.5a) and recognizable only for negatively chirped pulses (green and blue trace), it is much stronger for the fragment spectrum (fig. 3.5b). All fragment peaks grow significantly in size for longer pulses because more time is available for IC to proceed before ionization, resulting in increased fragmentation. This demonstrates that the Rydberg states up to 4p (2.05 eV peak) are populated by IC within the temporal range of the mentioned time constant. Note that the 4p states (2.05 eV peak) were determined as the highest relaxed states that lead to fragmentation for this photon energy (see fig. 3.4 and tab. 3.2).

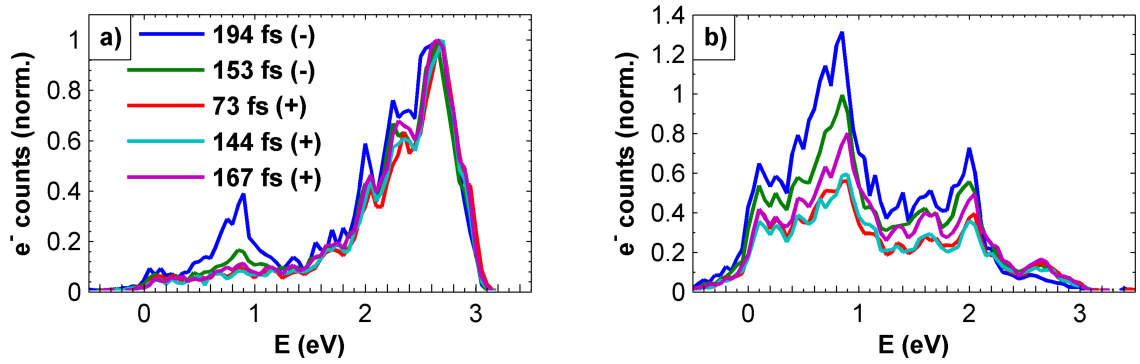

Figure 3.5: Acetone parent PEPICO (a) and fragment PEPICO (b) spectra obtained with chirped pulses of 3.14 eV photon energy, as given in the legend. Positive and negative chirps are indicated by plus and minus signs, respectively. Fragment and parent spectra for each pulse length are normalized to highest parent signal.

The increased fragmentation rate for longer pulses is also recognizable in fig. 3.6a, where the integrated fragment-to-parent ratio is plotted as function of the pulse length of positively (red) and negatively (blue) chirped pulses of 3.14 eV photon energy. It is immediately evident that the relaxation and fragmentation behavior is influenced by the sign of the chirp. Negatively chirped pulses, with the blue end of the spectrum advancing the pulse, lead to more efficient fragmentation than their positively chirped counterparts. For lower photon energies of 2.99 eV, in contrast, the integrated fragmentation ratio is independent of the chirp (not shown). This leads us to the following interpretation: The density of Rydberg states is higher in the energy region accessed with 3.14 eV, as compared to excitation with 2.99 eV (see tab. 3.1). With a higher density of states, the advancing blue part of a negatively chirped pulse is able to trigger different and more efficient relaxation pathways compared to the trailing red part. This is not the case if the average distance between states is larger than the spectral width of the pulse. Hence, the chirp dependence is observable with 3.14 eV but not with 2.99 eV photon energy.

We also note that different responses to positively and negatively chirped pulses is often a signature for coherent control of molecular processes. However, in this case the chirp dependence is based on pure energy arguments.

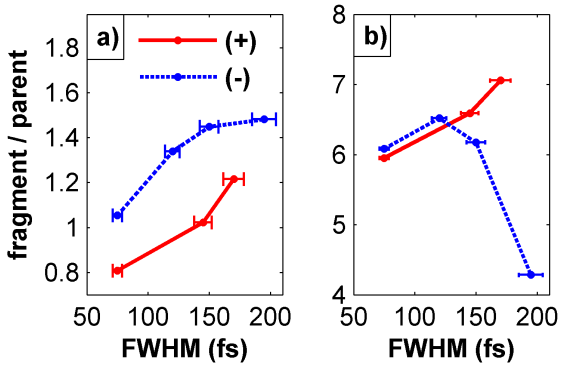

Figure 3.6: Fragment-to-parent ratio for positively (red) and negatively (blue) chirped pulses. In the left graph (a) the whole parent and fragment PEPICO spectra, as shown in fig.3.5, are integrated, while for the right graph (b) only the area beneath the 3p peak (0.9 eV) has been considered. The error bars indicate an estimated uncertainty of the FROG measurement.

The parent PEPICO spectrum in fig. 3.5a shows a clear increase of the 0.9 eV peak, corresponding to the 3p states, for the longest, negatively chirped pulses. This is remarkable, because almost 2 eV are converted to vibrational energy at this photon energy and a considerable fraction of the molecules does not undergo fragmentation. This is in accordance with our previous observations, where two-photon excitation (4.61 eV photon energy) and a time-delayed ionization (3.07 eV) lead to the same parent PEPICO peak for the 3p states, with a fragment-to-parent ratio of 2.7 [8]. We find that the height of the 3p parent peak increases by about 400 % within the observed pulse length range, while the corresponding fragment peak only doubles. This is clearly expressed by the fragment-to-parent ratio of the 3p peak, as shown in fig. 3.6b.
While the ratio initially increases equally with the pulse length for short pulses, it drops dramatically for longer pulses with negative chirp. In order to separate the influence of photon energies from that of the pulse chirp, we carried out pulse length variations with lower photon energies (2.99 eV), where this effect was not observed: The 3p parent signal is low and does not increase for negatively chirped pulses. Figure 3.7 shows the corresponding PEPICO spectra for these measurements. In figure 3.7a and 3.7b again spectra for 3.14 eV photon energy (395 nm) can be seen. The parent rise around 0.9 eV for negatively chirped pulses is clearly visible. However, in figure 3.7c and 3.7d, PEPICO spectra for corresponding pulse lengths with a photon energy of 2.99 eV (415 nm) are depicted. As can be seen, no parent rise for negatively chirped pulses is measured, but actually even a slight rise in parent signal for positively chirped pulses can be seen. We

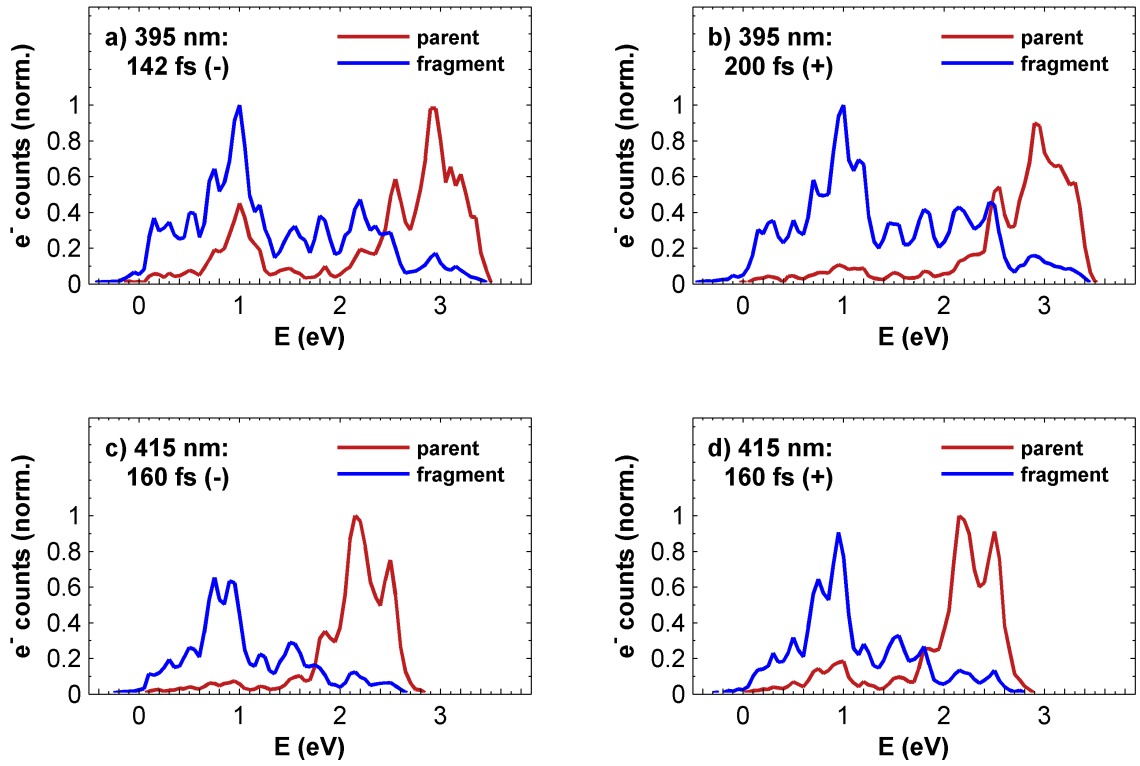

Figure 3.7: Comparison of the chirp direction-dependence for both 395 nm (compare figure 3.5) and for 415 nm. For 395 nm (a) and (b), again the rise in parent signal for negative chirps at 0.9 eV can be seen. This rise is not visible in the 415 nm negative chirp spectra (c) and (d).

explain this with the low pulse energies: a comparison of the width of the PEPICO spectra for the two wavelengths (figure 3.7) shows a significant lower high energy edge for measurements with 415 nm. The excitation for the positively chirped pulse happens with even lower energies, since in this case the red part of the spectrum is leading the pulse front. Therefore also a lower amount of vibrational energy is deposited into the molecule via the relaxation process and a lower part of the ionized molecules fragments.

These results lead us to the interpretation that a different IC relaxation pathway is accessed by the high photon energies at the beginning of the negatively chirped 3.14 eV pulse. Due to saturation, the high photon energies are able to activate these new pathways more strongly when they come at the beginning of a negatively chirped pulse as compared to a transform limited or positively chirped pulse. These pathways must proceed along different relaxation routes with different non-adiabatic couplings. Although the same amount of (or even more) energy is converted to vibrations, the redistribution of vibrational energy from the initially excited normal modes to other modes is different. Apparently, the CC stretch mode that finally leads to the breaking of the CC bond [23]

receives less energy in the relaxation paths originating from Rydberg states at about 9.5 eV, as compared to relaxation from slightly lower states. In this context it is important to note that no other fragmentation pathways, such as hydrogen separation from the acetone cation (mass peak at 57 amu) or the appearance of $C_2H_2O^+$ (42 amu), which would release energy, were identified. This can be seen in figure 3.8, where the detailed mass spectra for the acetone parent (58 u, left) and the fragment (43 u, right) from the pulse length variation measurements are depicted. The spectra for the different measurements are shifted to lower masses, which cause is not known and may be due to some charging effects of the repeller (compare with section 2.8.4). As can be seen, no mass peaks are detected for 1 atomic mass unit lower than the main 58 u and 43 u peaks, which would hint a hydrogen separation. However, for every measurement there exist some low signal mass peaks for exactly 1 and 2 mass units higher. Those peaks are due to carbon-13 isotopes, which have a natural appearance of about 1 % in all carbon on earth [31], which is also approximately the minimum ratio between the areas of the high C-12 and low C-13 peaks in the mass spectra.

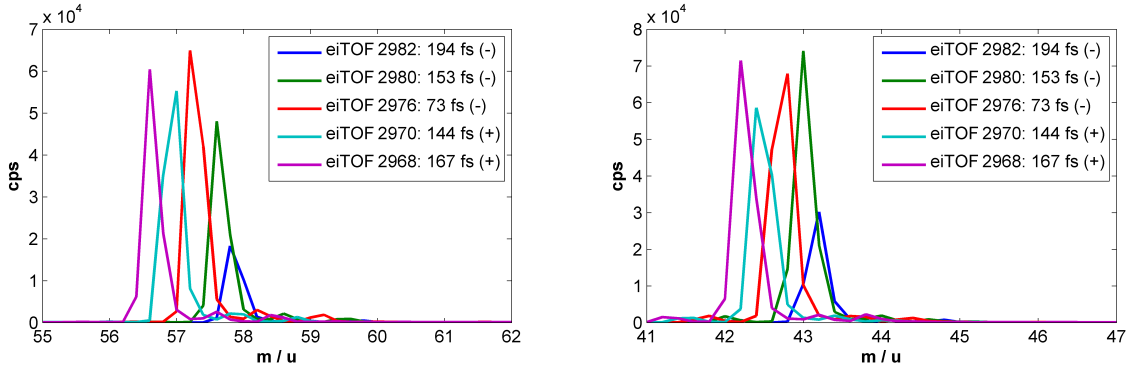

Figure 3.8: Detailed mass spectra for the acetone parent 58 u (left) and the fragment 43 u (right) for the different measurements presented in the pulse length scan (compare figure 3.5). The spectra shift slightly to the left (unknown reason) but more importantly, no significant mass peaks left of the main peaks, which would hint hydrogen separation, can be seen.

3.1.5 Pulse energy dependence

Finally, we determine the pulse energy dependence of the PEPICO fragment and parent peaks. Fragmentation in the ion can, in addition to energy conversion during IC in the neutral, be caused by absorption of additional photons after the ionization process [7], [32]. These two mechanisms cannot be distinguished in a single PEPICO spectrum. Figure 3.9 shows PEPICO spectra for 4 and 6 μJ. As can be seen, for electron kinetic energies lower than approximately 2.3 eV, the ratio between the parent (red) and fragment(blue) signal stays the same for both pulse energies. In the kinetic energy region above 2.3 eV, however, the ratio of fragment electrons clearly rises with respect to the parent signal.

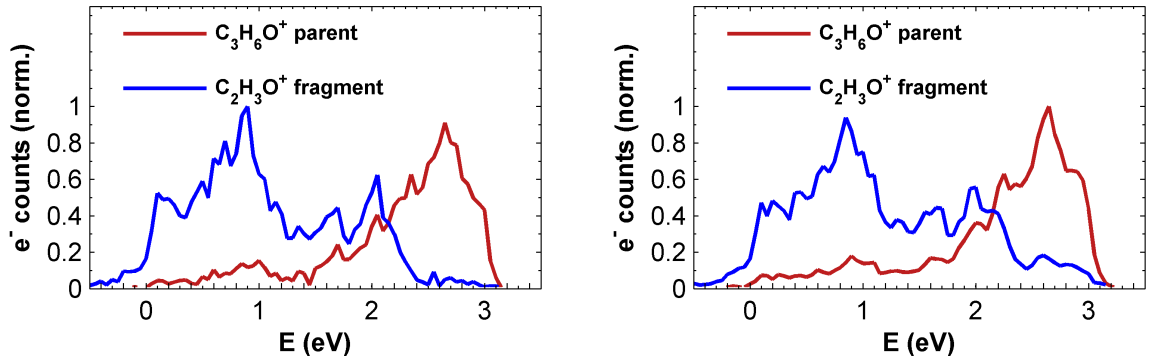

Figure 3.9: Two PEPICO spectra for different pulse energies: the left image shows a spectrum for 4 μJ pulse energy and the right image a spectrum taken with 6 μJ. As can clearly be seen, the ratio of the fragment signal above 2 eV is higher for the spectrum taken with higher pulse energy.

Since fragmentation due to subsequent excitation of the ion requires the absorption of at least one more photon, the two mechanisms show different pulse energy dependencies of the corresponding PEPICO signals. The number of photons involved in the ionization pathway leading to a certain ion can be obtained from the slope of the PEPICO energy dependence in a log-log plot, since the electron yield follows the relation:

$$electron\ yield \approx I^k,$$

with I the intensity and k the number of photons involved in the process. The inset of fig. 3.10 shows the pulse energy dependence of the fragment and parent PEPICO signals corresponding to the two main structures in the spectrum at 0.9 eV (3p) and at 2.7 eV (S_{n3}: 6p, 6d, 7s). Similar slopes were measured for the PEPICO signals over the whole PE energy range and are shown in fig. 3.10. In the energy region above 0.9 eV, where the PEPICO peaks have been assigned (tab. 1), slope values between three and four are obtained for both parent and fragment signals. These slopes represent the three-photon

excitation and one-photon ionization path (c.f., fig. 3.3), showing that no additional photon absorptions are involved in the process leading to both the parent and fragment ion. Non-integer slope values (fig. 3.10) can be explained by the laser focus intensity distribution in the ionization region in combination with saturation effects (if a major part of the electrons is already excited, more power cannot give the same signal rise hence the slope gets smaller). Above 2.2 eV a significant rise of the process order for the fragment ion is observed. This sudden increase can be compared to the results obtained above: Considering the average energy conversion threshold of $\Delta E_{vib} = (0.79 \pm 0.04)$ eV and the photon energy, fragmentation is expected for PEPICO signals below 2.1 eV ($E_{e,kin} = 4 \cdot h\nu - (IE + \Delta E_{vib})$, cf. tab. 3.2); thus, the fragment PEPICO signal above 2.1 eV, in particular the 2.7 eV fragment peak (fig. 3.2), must be related to subsequent excitation of the ion [7], [30], which explains the observed rise of the process order in fig. 3.10. The probability of the subsequent excitation channel is lower compared to the relaxation channel, as shown by the smaller fragment PEPICO signal at 2.7 eV compared to 2.0 eV and below (fig. 3.2).

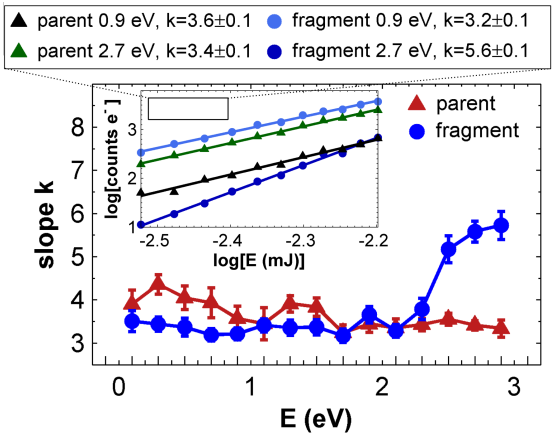

Figure 3.10: Pulse energy dependence of the parent (red triangles) and fragment (blue circles) PEPICO signals obtained with 3.14 eV photon energy. The signal is integrated over a bin size of 200 meV for each data point. The inset shows the actual energy dependence of parent (triangles) and fragment (circles) signals at the characteristic PE energies of 0.9 eV and 2.7 eV, in a log-log plot.

3.1.6 Summary and conclusions

The fragmentation behaviour caused by ultrafast non-adiabatic energy conversion from electronic to nuclear vibrational motion has been investigated in acetone molecules. We apply resonance enhanced four-photon ionization consisting of a three photon excitation to high-lying Rydberg states and a one-photon ionization (fig. 3.3). Although only a few states lie within the three-photon excitation bandwidth, the PEPICO spectra show that

a multitude of lower Rydberg states is populated. IC from the excited states to lower Rydberg states proceeds so fast, that population from the lower states is ionized within the same laser pulse. Energy conversion to vibrational modes during IC in combination with intramolecular vibrational energy redistribution leads to fragmentation of the molecule after the ionization event. By coincidence detection of the electron kinetic energy and the ion fragment for each ionization event, we were able to fully characterize the fragmentation behaviour and its dependence on the photon energy (excited state), pulse duration and chirp, as well as pulse energy. The activation energy for fragmentation, which we determine as the smallest amount of energy conversion required to facilitate fragmentation, was determined to be (0.79 ± 0.04) eV. Below this threshold the PEPICO spectra are dominated by parent signals and above this threshold fragment signals prevail. As the IC time constant is in the range of the pulse duration [8], the relaxation probability increases with longer pulses, yielding increased fragmentation. Our value for the activation energy agrees very well with results obtained from synchrotron experiments, where vibrationally excited cations are produced by one-photon ionization with photon energies above the IE [32], [33]. The breakdown curves for acetone ions and acetyl ions show that an excess energy of 0.79 eV above the IE results in fragmentation of about 90% of the acetone ions [33]. Furthermore, the calculated energy for dissociation of neutral acetone to an acetyl and a methyl radical is 3.61 eV, whereas for dissociation of the ground state acetone ion to an acetyl ion and a neutral methyl radical it is only 0.84 eV [34]. This is in perfect agreement with the experimental dissociation energy we observe and agrees with our interpretation that dissociation occurs after ionization and not ionization after dissociation, which could not be distinguished with less selective methods than PEPICO. Surprisingly, excitation energies of 9.5 eV with negatively chirped pulses lead to suppression of fragmentation despite a significantly higher energy conversion of 2.0 eV, as documented by a significant increase of the parent PEPICO signal associated to the 3p states. This indicates that additional relaxation pathways are available for excitation to increasingly higher Rydberg states, because these interact with higher valence states [22]. The redistribution of vibrational energy along these pathways seems to be different as it transfers less energy to the CC stretch mode, thereby reducing the fragmentation probability. Finally, we find with pulse energy variations that subsequent excitation of the ion, which also leads to fragmentation by depositing additional energy directly in the ion, plays a minor role. These results demonstrate that in the complex situation of multiple relaxation pathways, the high selectivity of PEPICO detection is a prerequisite to disentangle the pathways and observe their fragmentation behavior. This is the chase for applications based on multiphoton excitation.

CHAPTER 4

Appendix - software handling

In the following sections, the frequently used programs (mostly scripted in matlab) in the laboratory will be explained and listed. Most of them already existed at the starting point of this thesis, however a big part was modified or rewritten completely to better fit the daily requirements in the lab.

A Hardware control

Most of the computer assisted hardware in the laboratory is programmed and controlled via matlab, which allows a practical usage via the *Instrument Control Toolbox* and for example a control over a serial interface (RS 232).

A.1 Introduction: Matlab classes

A great part of the hardware-driving software is object-orientated programmed, meaning that a matlab class is defined which includes all the basic functions of the device and therefore an easy and clear way of usage. Listing 4.1 shows the basic syntax of the necessary code for such a matlab class with the program code of the counter (Stanford SR400) as example. The necessary code that defines the class is programmed in an extra matlab script. After the definition (class inherits from the class *handle*) and the addition of the *serialconn* property, different functions are defined that can be used to control an object of the class. The so called constructor is opened every time an object of the class is defined. In this case, the serial port with all its properties is defined (BaudRate, DataBits,

StopBits, Parity and Terminator) and the COM-port is opened. After the constructor, various functions can be defined that allow the software to send commands (*fprintf*) and to receive data (*fscanf*) with a serial communication via ASCII strings. At the end, a *delete* function (destructor) closes the serial port and clears the variable that was allocated to the object.

Listing 4.1: Example for the necessary code for a matlab class

```
classdef Counter < handle
    properties
        serialConn;
    end

    methods
        % constructor:
        function obj = Counter()
            % define serial parameters:
            obj.serialConn = serial('COM13');
            set(obj.serialConn,'BaudRate',9600);
            [...]

            % open serial port
            fopen(obj.serialConn);
            obj.startCounter();
        end

        % functions:
        function startCounter(obj)
            fprintf(obj.serialConn,'CS');
        end

        function [gateA, gateB] = getCurrentCounts(obj)
                fprintf(obj.serialConn,'QA');
                gateA = str2double(fscanf(obj.serialConn));
                fprintf(obj.serialConn,'QB');
                gateB = str2double(fscanf(obj.serialConn));
        end
        [...]

        % destructor:
        function delete(obj)
            fclose(obj.serialConn);
        end
    end
end
```

The created object can then be used in any matlab script. An example is depicted in listing 4.2. Importance has to be paid on the call of the destructor, otherwise the COM port stays open and the object cannot be used again (exception: if the object is opened not in a script, but rather a matlab function, the destructor is called automatically at the end of the function).

Listing 4.2: Examplecode for the usage of matlab objects

```
% open object of class counter (constructor):
c = Counter();

% get counts of the gates:
[countsA,countsB] = c.getCurrentCounts();

% close object (destructor)
c.delete();
```

A.2 Computer controlled hardware in the laboratory

Here a short list of the important hardware components in the laboratory is given, that are programmed and used with (matlab) software.

Camera/Beam profiler: Copy_of_profile_horver

The Camera class (*Camera.m*) communicates with the house-built beam profiler [16] and uses various functions of the *Image Acquisition Toolbox* to get the image data of the webcam. With the matlab function *Copy_of_profile_horver.m*, the data is read, plotted simultaneously and a gaussian fit curve is placed over the cross section of the maximum values. The fitted FWHM is given in px of the camera, where 1 px = 5.5 μm. In a previous version of the code, the video channel was opened every time before an image was loaded (via *videoinput*) and closed afterwards (*stop*). This led to long waiting times to get an image and was very tedious. Now the constructor of the class opens the videoinput and leaves it open. With the function *getImage* in the class, the image data is retrieved and can be manipulated. The destructor (*delete*) closes the video channel again.

Counter

The basics of the class script *Counter.m* for the Stanford Research Counter SR400 is given in listing 4.1. It is also controlled via serial USB and the complete communication protocol can be found in the SR400 manual. However, the function *getCounts* should be discussed in more detail and can be seen in listing 4.3. In order to take as little time as necessary, when one has long integration times, a *while*-loop compares the actual value on the counter with the value 0.1 s before. If the value changes, the new values are accepted and given. This also avoids that data is counted twice.

Listing 4.3: Code for the Counter function *getCounts*

```
function [gateA, gateB] = getCounts(obj)
    obj.resetCounts();
    [gateA_old, gateB_old] = obj.getCurrentCounts();
    pause(0.1);
```

```
5     run = true;
6     tic
7     while run && toc < 60
8         [gateA, gateB] = obj.getCurrentCounts();
9         run = gateA == gateA_old & gateB == gateB_old;
10        gateA_old = gateA;
11        gateB_old = gateB;
12        pause(0.1);
13    end
14    [...]
15 end
```

In the additional matlab function *CounterMode.m*, different gate-settings are and can be defined, that allow the fast switching between for example from electrons on GateA and ions on GateB (input 'A'), to acetyl fragment on GateA and acetone parent on GateB in repeller ion mode (input 'I'). The input values for the gate widths have to be given in μs and the program translates them into s, which is overloaded to the counter.

Spectrometer - OceanOptics

The spectrometer of type OceanOptics is controlled in the class *OceanOpctisSpectrometer.m*. For this, a java wrapper (called *OmniDriver*) needs to be included. The syntax and a short tutorial can be found on oceanoptics.com/faq, the driver files can be downloaded on oceanoptics.com/support (the urls are also documented in the matlab script). The spectrometer has as input value its integration time and uses basically only two functions, *getWavelengths* and *getSpectrum*, where the latter additionally returns a logical variable if the spectrum is saturated. For the spectrometer used (USB4000+) the saturation value was found to be 65535, however this depends of course on the CCD sensitivity and needs therefore to be adjusted for every new spectrometer. The device is called and the spectrum is plotted via the function *Spectrometer.m*. A figure with a permanently updating spectrum opens, the background of the figure turns red, if the spectrum is saturated. With the function *saveSpectrum.m*, the current input spectrum is saved and is numbered consecutively.

Shutter

Two little optical shutters were constructed for the automatic control of a switching between pump-probe mode, pump only and probe only for time resolved measurements. The shutters consist of servo motors (Conrad) that are controlled with an arduino microcontroller that is programmed with its own language (*servo_new*.c). In matlab, the class *Shutter.m* just opens a serial port and writes a character to the port. The function (*PPShutter(<char>)* opens the object, transfers the command (options for <char> are 'O' (both shutters closed/Off), 'P' (both shutters open/PumpProbe), 'R' (pRobe only shutter

open) and 'U' (pUmp only shutter open)) and again closes the serial port. A c program is running permanently on the arduino that translates the characters into angle-values for the servo motors.

Stage

The two Newport stage actuators (CONEX-LTA-HS) in the laboratory (one currently assembled in the FROG and one on the optical table for time-resolved pump probe measurements) are both controlled via a serial USB port. The class *Stage.m* needs in the constructor as input the number of the stage, 1 gives the port for the FROG stage and 2 the port for the stage on the optical table. The function *moveToPos.m* (see listing 4.4) allows the movement of the stage to a certain position (given in mm). The function opens a while loop and asks over the function *getPos()* the current position and compares it to the desired position. When the latter is reached, the while condition is negative and the loop breaks. Additional functions are *isDisabled*, which asks if the stage is disabled for motorized control over the software (returns bool = 1) or not (bool = 0). In order to get manual control, the stage actuator has to be disabled, however the functions *enable* and *disable* are called in the *Stage.m* constructor and destructor respectively and therefore manual control should be automatically guaranteed if the object is handled correctly.

Listing 4.4: Code for the Stage function *moveToPos*

```
function pos = moveToPos(obj, pos)
    string = strcat('1PA',num2str(pos, '%0.6f')); % sets position
    fprintf(obj.serialConn, string); % send to the motor
    pause(0.1);

    pos_old = -10;
    pos = 0;
    while pos ~= pos_old
        pos_old = pos;
        pos = obj.getPos();
        pause(0.1);
    end
    pause(0.1);
    pos = obj.getPos();
end
```

A.3 Peforming ion timescans: timescan_counts_2gates_v2

A nice example for the correct use of the hardware with matlab classes is the function *timescan_counts_2gates_v2.m*, which performs a time-resolved ion measurement and reads in the count-rates of the Stanford counter for each timestep. Parameters that need to be set are the begin- and end-position of the stage (*pos_begin* and *pos_end*):

This is done either directly via the position values on the stage (in mm), or, if one knows the overlap position, via the function *TimeToPos.m*, that translates time delays in stage position values. Additional parameters are the stepsize (given in mm) and the integration time of the counter (in s). Listing 4.5 shows the basic code for the program. The current counts are plotted and at the end a gaussian fit curve is drawn over the overlap region.

Listing 4.5: Code for the ion timescan: timescan_counts_2gates_v2

```
% define parameters:
stepsize= 0.0015;
intTime = 2;

pos00 = 27.357;
pos_begin = TimeToPos(0.5, pos00);
pos_end = TimeToPos(-0.5, pos00);

% open hardware:
stage = Stage(2);
counter = Counter();

% define positions:
n = round(abs(pos_end-pos_begin)/stepsize);
pos_vector = linspace(pos_begin,pos_end,n+1);
[...]

% perform timescan:
for j=1:numel(pos_vector)
    pos_cps(1,j) = stage.moveToPos(pos_vector(j));
    [pos_cps(2,j), pos_cps(3,j)] = counter.getCounts();
    [...]
end
```

Especially the conditions in the while loops (described above in listing 4.3 and 4.4) in the two hardware classes of the stage and the counter prevent here for example a wrong counting (e.g. counting at false positions when the iteration time is quite long).

A.4 Taking and Retrieving FROG traces: SD_Quaq and FROG3.exe

The matlab function *SD_Quaq* takes a FROG-trace and saves it in the desired format, so that the external program *FROG3.exe* can use it and perform the retrieval algorithm (see section 2.4). The zero position (evaluated manually), the width of the desired FROG trace (given in ps), the desired step size (in ps) and the central wavelength of the spectrometer have to be given as input values. The program constructs objects of the classes stage (1) and spectrometer and initializes all variables. The format of the output file (the FROG trace) to be retrieved from the *FROG.exe* program has to have the following form:
The width and the height of the FROG trace has to be an integer number. Further, the FROG retrieval needs horizontally and vertically equally spaced datapoints. This is a

[tracewidth (px)] \t [traceheight (px)] \t [fs/px] \t [nm/px] \t [center wavelength] \n
RAW DATA MATRIX (1st dim (col): spectrum, 2nd dim (row): time-delay)

problem for the wavelength-values due to the fact that Ocean Optics spectrometers are not equally sensitive in all wavelength regions and produce a non-equally spaced vector of wavelengths. Therefore *SD_Quag.m* performs also a binning routine (function *binning.m*, see B.4), where it splits the spectrum into 1600 equally spaced wavelength bins and redistributes the signal appropriately. The signal is plotted as a function of wavelength and time-delay in a two-dimensional plot (*imagesc*), additionally the integrated spectrum (over all wavelengths) and the current wavelength spectrum are plotted in subplots. The loop over the steps of the SD_Quaq routine can be seen in listing 4.6.

Listing 4.6: Measurement loop in the SD_Quaq function

```
[...]
for j = 1:numel(steps)
    % move to desired position and get spectrum
    steps(j) = stage.moveToPos(steps(j));
    [spectrum, isSaturated] =  spectrometer.getSpectrum();

    % perform binning in wavelength-space
    [~, spectrum_bin] = binning(fkt, wavelengths_bin,...
                            wavelengths, spectrum, Jac);

    % save spectrum to variable
    FROG_Matrix(:,j) = spectrum_bin;
    int_spectrum(j) = sum(spectrum_bin);

    % plot spectra
    set(p_int_spectrum,'YData',int_spectrum);
    set(image_frogtrace, 'CData',FROG_Matrix);
    set(p_spectrum,'YData',spectrum_bin);

    % saturation:
    if isSaturated
        set(fig,'Color','r')
    end
    drawnow;
end
[...]
```

At the end a gauss-fit is performed on the integrated autocorrelation curve and the FWHM is given. The appropriate FROG-trace axis is transformed to the time-domain and is saved in the desired format to be able to perform the retrieval algorithm. All recorded FROG traces are saved and numbered consecutively.
A screenshot of the used retrieval program *FROG3.exe* with typical set values is given in figure 4.1. High Grid Sizes give a lower FROG error, however the iteration takes longer. As Data source *Experimental FROG trace* has to be set and *SD* (Self-Diffraction) is the

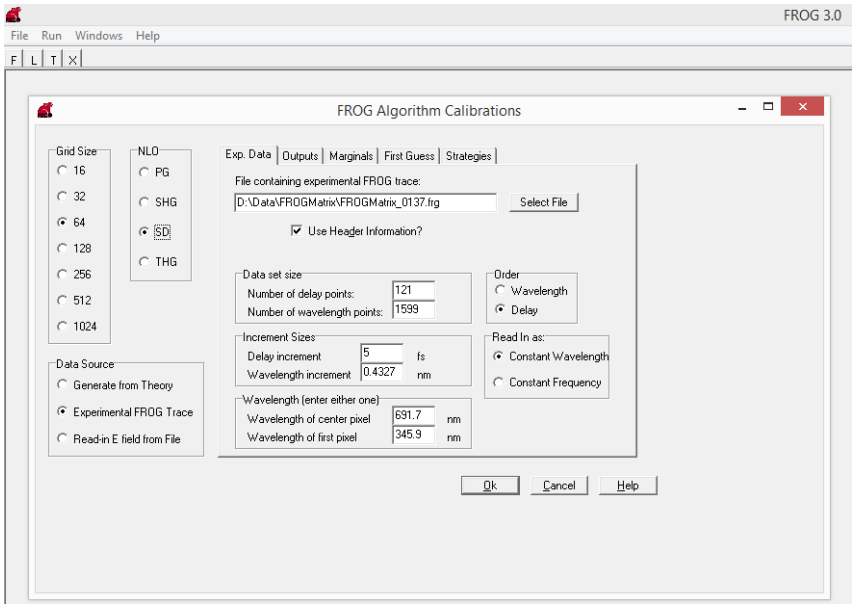

Figure 4.1: The FROG retrieval program with typical set values for a FROG trace.

non-linear optical effect. The file with the desired FROG trace number has to be selected and the header information should load the correct parameters. As Order, *Delay* and as Read In, *Constant Wavelength* have to be set. The retrieval is best performed with a noise subtraction of *Full Spectrum*. Via *Grid Data* and then *Start* the retrieval algorithm is started.

B Time-Of-Flight management

In this section, the codes for taking and analysing Time Of Flight spectra are explained. Because the main function for this, *RMT_v2.m*, was quite adjusted during the working period of this thesis, it is discussed and explained in more detail in the following.

B.1 Taking TOF spectra: RMT_v2

Measurements with the Time-of-Flight spectrometer (compare experimental part 2.2) are taken with the matlab function *RMT_v2.m*. The measurement principles for the different detection modes (electrons, ions, PEPICO) are explained in the master thesis of Markus Bainschab [14], special attention should be paid on the origin of the variables *HVoff* and *Delta_HVoff* (time points for the off-switch of the high voltage). In the first version of the program (*RMT.m*), the time-of-flight traces were saved as raw data and analysed with respect to counts afterwards. Since a loading of that amount of data (>5 GB for a $1 \cdot 10^6$ scan), that consisted to an overwhelming part anyway of zeros, took quite a long

time with matlab and also with a c-script, the program *RMT* was rewritten. Now, a c-subroutine (*findpeak_v2.c*) evaluates every time trace and looks for peaks (compare to section 2.2). The raw data of the time-traces are discarded and the peaks are saved to matlab variables, which at the end are again saved with another c-subroutine (*writefile.c*) to .txt files (hist and list files, see section 2.2).
The function *RMT_v2* requires several variables to be set:

- **runs:** number of time-traces (laser shots) that shall be recorded (typical values: 1e4, 1e5 or 1e6)
- **eOi:** sets the mode for the spectra to be measured, 2 is for 1 GS, 4 is for 2 GS (more detailed: different setup files for the desired measurement modes are loaded)
- **CFD:** if set to 1, constant fraction discriminator is used, if 0, constant value (see section 2.2)
- **saveRawData:** if set to 1, all time-traces (and additional the averaged ones for every trace) where hits were recorded are saved, to be able to analyse them with *eiTOF_fileread_traces.m*.
- **discE/discI:** discriminator levels for electron/ion detection
- **diseE/I_afterPeak:** discriminator levels for detection after a peak was detected
- **discTime:** time for which the afterpeak-discriminators are taken
- **Nmean:** number of traces for the calculation of the subtracted mean traces

At first, the 'eiTOF_info' file (contains all set variables) is created and the Gage Cobra fast digitizer card is initialized (see its documentation for details). The times for the switching of the high voltage are set (separates ion and electron detection) and afterwards the necessary input data for the *findpeak_v2.c* algorithm is initialized (see listing 4.7).

Listing 4.7: Initialized variables in RMT_v2 for the findpeak_v2.c routine

```
% vectors for total-/electron-/ion-histogram (hist-files)
% and hitlists (peakpos => list-files)
histspec = zeros(datalength, 1);
histspec_e = zeros(HVoff - delta_HVoff, 1);
histspec_i = zeros(datalength - HVoff - delta_HVoff, 1);
peakpos = zeros(runs, 100);
peakpos_e = zeros(runs, 100);
peakpos_i = zeros(runs, 100);

% necessary data for the findpeak_v2.c routine
peakfinder_input_data = [...
```

```
12          samplerate;...
13          HVon;...
14          HVoff;...
15          delta_HVoff;...
16          chanInfo.InputRange*0.001;...
17          acqInfo.SampleResolution;...
18          size(peakpos,1);  ...
19          numel(peakpos);...
20          discE;...
21          discE_afterPeak;...
22          discI;...
23          discI_afterPeak;...
24          discTime;...
25          CFD]';
```

Afterwards, in a loop over all runs, one timetrace is recorded each step and its voltages are set to the variable *data*. The digitizer card has a resolution of 8 bit (256 values) and records the analogous voltage signal between -0.5 and +0.5 V (0 and 1 V with 127 (4 bit - 0.5 V) offset). Hits on the MCP produce negative voltage peaks and can therefore be recalculated to positive voltage values via:

$$signal[V] = signal[digital] \cdot 0.5 \cdot \frac{range(=1V)}{resolution(=-128)}$$

This is done in the *findpeak_v2.c* routine. In the matlab code, the first Nmean curves are averaged and the *findpeak_v2.c* routine is called. In the code, a for-loop scans over all datapoints in the time-trace. Depending on the time-position, different discriminator levels are chosen for electrons and ions and it is always checked, if a peak has been detected within this same timetrace in the timeframe of discTime. If so, the *afterpeak* discriminators are chosen, in order to avoid double counts through back-oscillations in the cable (compare 2.2). Listing 4.8 shows the code for a peak detection via CVD. A peak is detected, if the voltage level rises above a certain threshold (*minpeakheight*, which corresponds to the set discriminator level).

Listing 4.8: example for peak detection in *findpeak_v2.c*

```
1 /* peak found (CVD)? */
2 if
3 (((data[i - 2*(int)samplerate]-dataMean[i - 2*(int)samplerate])
4 *0.5*range/resolution < minpeakheight) &&
5 ((data[i - 2*(int)samplerate + 1]-dataMean[i - 2*(int)samplerate + 1])
6 *0.5*range/resolution > minpeakheight)){
7       peakFound = true;
8 }
```

If a peak is found, its position is saved to the vectors *histspec* and *peakpos*, which are again passed back to the *RMT_v2.m* function. Note that there exist three different hist and peakpos (list) arrays: for all counts, for electrons and for ions. The total hist/list file

is split in the time domain into the other two, with the time separation done at the time when the high voltage is switched off (HVoff). At the end of the loop over all laser shots (runs), those vectors are saved as the corresponding hist- and list- files (compare section 2.2.3). Because the generation of these files with matlab can take quite some time, it is again outsourced to a c-script called *writefile.c*. The important part of the script is shown in listing 4.9.

Listing 4.9: write hist and list files with *writefile.c*

```
/* scan over all rows of vector */
for (i=0; i < mrows; i++){
   /* if hist file, save number of counts for each time (row) */
   if (isHist == 1) {
      fprintf(fidin,"%d\n",(int)data[i]);
   /* if list file: */
   } else {
      /* check for number of counts for each shot (row) */
      int peakcount = 0;
      for (j = 0; j < ncols; j++){
         if(data[i+j*mrows] != 0){
            peakcount++;
         } else {
            break;
         }
      }
      /* write shot number (col 1) and number of counts (col 2) */
      fprintf(fidin,"%d %d ", (int) (i+1), (int)peakcount);

      /* write time position of counts (col 3 - col ..)*/
      for (j = 0; j < peakcount; j++){
         fprintf(fidin,"%d ",(int)data[i+j*mrows]);
      }
      fprintf(fidin,"\n");
   }
}
```

At the end of each execution of *RMT_v2*, the function *FileDiagnostics.m* is called (see next chapter).

B.2 FileDiagnostics

The function *FileDiagnostics.m* analyses each TOF measurement and returns the most important parameters. Most importantly, especially after measuring in PEPICO mode, it calls *Stert.m* (and its subroutine *HitMat.m*), which fits and calculates the mean number of ionization events per laser shot (λ), the true-to-false ratio and the electron and ion detection efficiencies. *Stert.m* uses the total number of counts as well as the number of 1:1 coincidences (one ion and one electron) which it reads out of the hist- and list-files. The exact derivations and calculations can be found in refs. [14] and [18]. Additionally,

FileDiagnostics.m returns the mean number of electron and ion hits per second, the samplerate and the number of runs, that were recorded.

B.3 Examining time traces: eiTOF_fileread_traces

If one has saved the raw data time-traces in *RMT_v2.m* (variable *saveRawData* set to 1), they can be evaluated and analysed with the program *eiTOF_fileread_traces_v3.m*. The variables *discE* and *discI* allow to display the correct discriminator levels in the timetrace. The program shows in the upper subplot the raw time-traces (the HV-switch noise is quite high) and in the lower subplot the raw data subtracted with the averaged one, the latter has been taken for the evaluation with *findPeak_v2.c*. This program allows to get various insights into the data collection and should be used every now and then to adjust the discriminator levels (set in *RMT_v2*). Also several problems, e.g. the appearance of double peaks (back-oscillations in cable - see 2.2) or a signal change from the MCP (compare 2.8.2) can be figured out and analysed. It is recommended to compare the raw data traces every now and then with the corresponding list files to check a correct data collection.

B.4 Data evaluation

Once the TOF-data are recorded and stored in the hist and list files, various programs allow the evaluation. Because loading the hist- and list files with matlab became kind of tedious (>30 s for every file), c-scripts were written which fulfill this task much faster.

read_list_file.c and read_hist_file.c

- **read_hist_file.c:** Needs as input the filename and optional 'e' or 'i', depending on which hist-file shall be read. The output is a histogram vector, with the measured counts in each line that corresponds to the time step.

- **read_list_file.c:** Needs as input the filename, the number of count events to be given per shot (*numCoinMax*) and optional 'e' or 'i'. It returns a vector *numhits*, that contains the number of hits in each line (so each line was a laser shot). Additionally, the array *hitTimeList* contains for each line/shot *numCoinMax* measured hit times (dimension: runs x numCoinMax).

The hist-file is evaluated when only electron or only ion spectra are needed, since the kinetic energy- and the mass-spectra are nothing else than transformed time-histograms (see secs. eTOFplot B.4 and iTOFplot B.4). The list-file is called for the evaluation in

PEPICO mode, especially when 1:1 coincidences need to be evaluated (see sec. sortElectronsInMassWindows B.4). In the latter case, the variable *numCoinMax* (set to value 1) is responsible, that only events with 1 electron or 1 ion are loaded.

binning.m

The time-of-flight measurements give only histograms in the time-frame, that need to be recalculated into the energy or mass domain, for electrons and ions respectively. Also because of the non-linear relationships between time and energy/mass, the measured counts have to be sorted into new equidistant windows in the energy/mass domain. The matlab function *binning.m* does this in a general way, because it allows the execution of a signal transformation and sorting for an arbitrary transformation function (e.g. E(t) or m(t)). Here (and also in the programs) the variables are always called E and t, however the function works for arbitrary relations (e.g. m and t, but also $\Delta\lambda_1$ and $\Delta\lambda_2$ - see SD_quaq A.4).
Input values:

- **Efkt:** functional form of the new function, dependent on t
- **E_edges:** the new windows, in which the signal has to be sorted
- **t_vec:** the old windows (time-steps), for which the signal exists
- **sig_t:** histogram in the time-frame (counts for t_vec)
- **Jac:** Jacobi function of *Efkt*, meaning $|\Delta E/\Delta t| = |\delta E/\delta t|$
- **C:** covariance matrix, important for an error estimation (not only, but also after Bayes evaluation); see master thesis of Pascal Heim [15]

Output values:

- **E_vec:** new values of bins/positions in the histogram
- **sig_E_bin:** signal (counts) for each value
- **t_vec:** the old windows (time-steps)

Listing 4.10 shows the important steps in the binning function. Excluded is the calculation of the covariance matrix, which is also done. At first the time vector is transformed to energy values, which are then sorted in the desired energy bins. Afterwards the signal is transformed over the 1-dimensional probability space relation:

$$f(t)\Delta t = f(E)\Delta E$$

which is however just an continuous approximation for a discrete signal. Then for each bin, the mean number of counts that fall into it is calculated and afterwards the counts are again renormalized to the total signal, because the total number of counts has to stay the same in energy and time-space.

Listing 4.10: The binning.m routine

```
% calculate new E positions and transform t vector
E_vec = 0.5*(E_edges(1:end-1)+E_edges(2:end));
t_to_E = Efkt(t_vec);

% transform variables, ask which E(t) is in which E-bin
[~, bin_E] = histc(t_to_E, E_edges);

% transform signal/counts into E-space
sig_E = sig_t.*Jac(t_to_E);

% calc. mean of each bin
sig_E_bin = nan(size(E_vec));
for i = 1:numel(E_vec)
    sig_E_bin(i) = mean(sig_E(bin_E == i)); % [counts/t]
end

% renormalize
fac = sum(sig_t)/nansum(sig_E_bin));
sig_E_bin =  fac.*sig_E_bin;
```

eTOFplot

The function *eTOFplot.m* allows to plot either the full electron kinetic energy spectrum of the measurement, but can also give only the spectrum of a specific electron datavector (*data_e*, for example from coincidence electrons to a certain ion fragment). The latter is used in *FRATI_plot_multi_step* and *sortElectronsInMassWindows*, see sec. FRATI_plot_multi_step B.4.
Important parameters in eTOFplot are the variables *t0*, which names the time offset between the digitizer trigger and the time of ionization, and *lft*, which is the length of the flight tube. The exact values of these two should be calibrated every now and then with an ATI-measurement on argon, which is described in detail in the thesis of Markus Bainschab, chapter 2.2.1 (see ref. [14]).

Input value for eTOFplot is at first the variable *filenameOrOptions*. In the case of normal electron spectra plotting, it has to be the filename as a string, in the case for plotting a certain electron spectrum (e.g. only coincidences), the variable has to be named 'data_e' as string and additionally the variables *data_e* (contains all electron flight times to be plotted) and *samprate* have to be given as input variables. The other input variables

can be the energy-resolution *en* and an energy offset *enplotff*, as well as the time-domain datavector *t_vec*.

At first, out of the signal histogram (*sig_t*, either gotten with *read_hist_file.c* or calculated with *data_e* and the time-vector *t_vec*), the binning function is performed. For this, the functions *Efkt* and *Jac* as seen in listing 4.11 are defined. After the binning, the spectrum is plotted.

Listing 4.11: Performing the binning in eTOFplot

```
% prepare for binning: define energy function and jacoby
E_vec = eps:en:Emax;
Efkt = @(t) tmc./t.^2;
Jac = @(E) 0.5*sqrt(tmc)*E.^(-3/2);

for i = 1:size(sig_t,1)
   % binning
   [centers(:,i), counts(:,i), ~] = binning(Efkt, E_vec,...
                                    t_vec, sig_t(i,:), Jac);
end
```

In the whole function (same goes for iTOFplot, see next chapter), there should be special attention on the handling of units. The time-steps in the time-traces are, depending on the samplerate, for example 1 ns or 0.5 ns. Also experimental parameters like t0, HVon or HVoff are given in ns. However for better overview, all formulas (e.g. *Efkt*) are programmed for times given in s (transformation factor *tmc*).

iTOFplot

The function *iTOFplot.m* is very similar to *eTOFplot.m*. It performs a binning from the time-space into the mass space of the ions. The most important input variable to define is the voltage U, which represents the high voltage potential of the repeller at the laser focus (spot of ionization). It has to be calibrated every know and then with a known mass spectrum (e.g. xenon, compare Bainschab [14] chapter 2.3.1). Again the hist vector is generated for the two cases, when the ion times are given directly (the variable *filenameOrOptions* has to be set to 'data_i') or over the filename and *read_hist_file.c*. After that, binning is performed, which is depicted in listing 4.12. The mass resolution is currently set to 0.1 u, which is the step in the vector that is overloaded to the binning function.

Listing 4.12: Performing the binning in iTOFplot

```
% constant factor
tmc = 2*1.6e-19*U/(lft^2*1.66e-27);
% prepare for binning: define mass function and jacoby
mfkt = @(t) tmc*t.^2;
```

```
5     Jac = @(m) 0.5./sqrt(tmc*m);
6
7     % binning (mass resolution: 0.1 u)
8     [centers, counts] = binning(mfkt, 0:.1:mMax, t_vec, sig_t, Jac);
9
10    % calculate masses of data_i (for output to e.g. PEPICO eval.)
11    if strcmp(filenameOrOptions, 'data_i')
12       sig_M = mfkt(data_i);
13    end
```

After the binning, the data is plotted. If the ion times have been given directly (*filenameOrOptions* is at 'data_i'), the masses of the array data_i are calculated and are given as output of the function, to be used for example in *sortElectronsinMassWindows* B.4).

FRATI_plot_multi_step

The program *FRATI_plot_multi_step.m* (the name has historic reasons and stands for Fragment Resolved ATI), performs the evaluation of a combined electron/ion measurements with the PEPICO method. In its current form, it combines *sortElectronInMassWindows*, *eTOFplot* and *iTOFplot*. Its input parameters are the filenumber, the high voltage U and most importantly the mass intervals, for which electron spectra should be evaluated in PEPICO mode. Additional parameters that need to be set are again the energy offset *enplotoff* and the resolution *en*. FRATI_plot_multi_step.m calls *sortElectronsInMassWindows*, which looks for coincidence counts and sorts the electron counts into the desired mass intervals of the ions. Afterwards, the given data is evaluated and plotted with eTOFplot, with the direct handover of the flight times data of the desired electrons (*filenameOrOptions* is at 'data_e').

sortElectronsInMassWindows

This function loads at first the time-of-flight values of electron and ion data of the desired file in the subroutine *loadData* (with *read_list_file.c*). Here also the numbers of hits for every shot are stored in the vectors *numhits_e* and *numhits_i*. With these vectors, a logical variable is created to assign the shots where a coincidence (1 electron and 1 ion) was detected. With the ion data (*data_i*), iTOFplot is called that calculates the corresponding masses (and plots the mass spectrum). After that, the electrons are sorted into the mass intervals that are given and are stored in the *data_e* array, which is given to the output to be plotted in the *FRATI_plot_multi_step.m* program. All these steps are shown together in listing 4.13.

Listing 4.13: Coincidence evaluation in sortElectronsInMassWindwos

```
1     % find coincidences
2     L = numhits_e == 1 & numhits_i == 1;
```

```
3     [...]
4
5     % take only coincidence data
6     data_e = nan(sum(L), size(intervals, 1));
7     time_e = time_e(L);
8     data_i = time_i(L);
9     [...]
10
11    % convert ion flight times to masses
12    [~, ~, masses_i] = Copy_of_iTOFplot('data_i', U, intervals, 100,...
13                                        data_i, samprate);
14
15    % go over all intervals:
16    for i = 1:size(intervals,1)
17       % find coincidences in this mass window
18       L = intervals(i,1) <= masses_i & masses_i < intervals(i,2);
19       tmp = time_e(L);
20
21       % select coincidence electrons in this mass window
22       data_e(1:numel(tmp), i) = tmp;
23       [...]
24    end
```

Covariance_part

Just for completeness, it is mentioned that additional to the PEPICO detection method, the data can also be evaluated with convariance mapping, so basically by determining, which electron energies come with which ion masses at a high probability. This evaluation method however was rarely used during the working period of this thesis. The advantages and principles of covariance evaluation are better described in refs. [12] and [14]. The matlab function *Covariance_part.m* peforms a covariance evaluation of the data, but is however not at the current status of sub-programs (for example, the hist and list files are loaded directly with matlab, also the binning is done directly in the script). If the covariance method should at some time come to a wider usage again, the code should also be rewritten because of speed advantages and code consistency in the lab.

Bibliography

[1] RW Schoenlein, LA Peteanu, et al. "The first step in vision: femtosecond isomerization of rhodopsin". In: *Science* 254.5030 (1991), p. 412.

[2] C.E. Wayne and R.P. Wayne. *Photochemistry*. Ocp Series. Oxford University Press, 1996. ISBN: 9780198558866.

[3] Nobelprize.org. Nobel Meida AB 2014. *Press Release: The 1999 Nobel Prize in Chemistry*. 2014. URL: http://www.nobelprize.org/nobel_prizes/chemistry/laureates/1999/press.html.

[4] Albert Stolow, Arthur E Bragg, and Daniel M Neumark. "Femtosecond time-resolved photoelectron spectroscopy". In: *Chemical reviews* 104.4 (2004), pp. 1719–1758.

[5] IV Hertel and W Radloff. "Ultrafast dynamics in isolated molecules and molecular clusters". In: *Reports on Progress in Physics* 69.6 (2006), p. 1897.

[6] Andrey E Boguslavskiy et al. "The multielectron ionization dynamics underlying attosecond strong-field spectroscopies". In: *Science* 335.6074 (2012), pp. 1336–1340.

[7] Péter Sándor, Arthur Zhao, Tamás Rozgonyi, and Thomas Weinacht. "Strong field molecular ionization to multiple ionic states: direct versus indirect pathways". In: *Journal of Physics B: Atomic, Molecular and Optical Physics* 47.12 (2014), p. 124021.

[8] Paul Maierhofer, Markus Bainschab, Bernhard Thaler, Pascal Heim, Wolfgang E. Ernst, and Markus Koch. "Disentangling Multichannel Photodissociation Dynamics in Acetone by Time-Resolved Photoelectron–Photoion Coincidence Spectroscopy". In: *The Journal of Physical Chemistry A* 120.32 (2016). PMID: 27459051, pp. 6418–6423. DOI: 10.1021/acs.jpca.6b07238. eprint: http://dx.doi.org/10.1021/acs.jpca.6b07238. URL: http://dx.doi.org/10.1021/acs.jpca.6b07238.

[9] Rick Trebino, Kenneth W DeLong, David N Fittinghoff, John N Sweetser, Marco A Krumbügel, Bruce A Richman, and Daniel J Kane. "Measuring ultrashort laser pulses in the time-frequency domain using frequency-resolved optical gating". In: *Review of Scientific Instruments* 68.9 (1997), pp. 3277–3295.

[10] R. Pashotta. *Article on 'streak camearas in the Encyclopedia of Laser Physics and Technology*. 2017. URL: https://www.rp-photonics.com/streak_cameras.html.

[11] Wikipedia. *Optical autocorrelation — Wikipedia, The Free Encyclopedia*. [Online; accessed 6-February-2017]. 2016. URL: https://en.wikipedia.org/w/index.php?title=Optical_autocorrelation&oldid=754759374.

[12] Paul Maierhofer. "Femtosecond Photodissociation Dynamics in Molecules studied by Time-Resolved Photoelectron-Photoion-Coincidence Spectroscopy". Master Thesis. Institute of Experimental physics, Graz University of Technology, 2016.

[13] Wikipedia. *Spectral phase interferometry for direct electric-field reconstruction — Wikipedia, The Free Encyclopedia*. [Online; accessed 7-February-2017]. 2016. URL: https://en.wikipedia.org/w/index.php?title=Spectral_phase_interferometry_for_direct_electric-field_reconstruction&oldid=719843142.

[14] Markus Bainschab. "Multiphoton Ionization Channels in Molecules Investigated by Photoelectron-Photoion-Coincidence Spectroscopy". Master Thesis. Institute of Experimental physics, Graz University of Technology, 2016.

[15] Pascal Heim. "Femtosecond Photodissociation Dynamics in Molecules studied by Time-Resolved PEPICO". Master Thesis. Institute of Experimental physics, Graz University of Technology, 2017.

[16] Christian Gösweienr. "Konstruktion und Charakterisierung eines Laserstrahlprofilmessgerätes". Bachelor Thesis. Institute of Experimental physics, Graz University of Technology, 2012.

[17] Franz Koberg. "Femtosecond photoelectron and photoion spectrometer". Bachelor Thesis. Institute of Experimental physics, Graz University of Technology, 2015.

[18] Stert, V., Radloff, W., Schulz, C. P., and Hertel, I. V. "Ultrafast photoelectron spectroscopy: Femtosecond pump-probe coincidence detection of ammonia cluster ions and electrons". In: *Eur. Phys. J. D* 5.1 (1999), pp. 97–106. DOI: 10.1007/s100530050234. URL: http://dx.doi.org/10.1007/s100530050234.

[19] Light Conversion. *OPerA-Solo with TOPAS technology*. User's Manual. Light Conversion, 2015.

[20] Yehuda Haas. "Photochemical α-cleavage of ketones: revisiting acetone". In: *Photochemical & Photobiological Sciences* 3.1 (2004), pp. 6–16.

[21] Vincent Tagliamonti, Péter Sándor, Arthur Zhao, Tamás Rozgonyi, Philipp Marquetand, and Thomas Weinacht. "Nonadiabatic dynamics and multiphoton resonances in strong-field molecular ionization with few-cycle laser pulses". In: *Physical Review A* 93.5 (2016), p. 051401.

[22] Aparna Shastri and Param Jeet Singh. "Vibrational modes in excited Rydberg states of acetone: A computational study". In: *Journal of Quantitative Spectroscopy and Radiative Transfer* 173 (2016), pp. 92–105.

[23] Eric W-G Diau, Carsten Kötting, Theis I Sølling, and Ahmed H Zewail. "Femtochemistry of Norrish Type-I Reactions: III. Highly Excited Ketones—Theoretical". In: *ChemPhysChem* 3.1 (2002), pp. 57–78.

[24] M Nobre et al. "The VUV electronic spectroscopy of acetone studied by synchrotron radiation". In: *Physical Chemistry Chemical Physics* 10.4 (2008), pp. 550–560.

[25] Aparna Shastri, Param Jeet Singh, BN Raja Sekhar, R D'Souza, and BN Jagatap. "The role of torsional modes in the electronic absorption spectrum of acetone". In: *Journal of Quantitative Spectroscopy and Radiative Transfer* 113.12 (2012), pp. 1553–1565.

[26] Theis I Sølling, Eric W-G Diau, Carsten Kötting, Steven De Feyter, and Ahmed H Zewail. "Femtochemistry of Norrish Type-I Reactions: IV. Highly Excited Ketones—Experimental". In: *ChemPhysChem* 3.1 (2002), pp. 79–97.

[27] Nerijus Rusteika, Klaus B Møller, and Theis I Sølling. "New insights on the photodynamics of acetone excited with 253- 288nm femtosecond pulses". In: *Chemical Physics Letters* 461.4 (2008), pp. 193–197.

[28] DHA t Steege, AC Wirtz, WJ Buma, et al. "Vibronic coupling in excited states of acetone". In: *Journal of Chemical Physics* 116.2 (2002), pp. 547–547.

[29] Péter Sándor, Vincent Tagliamonti, Arthur Zhao, Tamás Rozgonyi, Matthias Ruckenbauer, Philipp Marquetand, and Thomas Weinacht. "Strong Field Molecular Ionization in the Impulsive Limit: Freezing Vibrations with Short Pulses". In: *Physical review letters* 116.6 (2016), p. 063002.

[30] Arthur Zhao, Péter Sándor, Tamás Rozgonyi, and Thomas Weinacht. "Removing electrons from more than one orbital: direct and indirect pathways to excited states of molecular cations". In: *Journal of Physics B: Atomic, Molecular and Optical Physics* 47.20 (2014), p. 204023.

[31] Wikipedia. *Carbon-13 — Wikipedia, The Free Encyclopedia*. [Online; accessed 1-December-2016]. 2016. URL: https://en.wikipedia.org/w/index.php?title=Carbon-13&oldid=752424523.

[32] Emma E Rennie, Anne-Marie Boulanger, Paul M Mayer, David MP Holland, David A Shaw, Louise Cooper, and Larisa G Shpinkova. "A photoelectron and TPEPICO investigation of the acetone radical cation". In: *The Journal of Physical Chemistry A* 110.28 (2006), pp. 8663–8675.

[33] Andras Bodi, Tomas Baer, Nancy K Wells, Daniel Fakhoury, David Klecyngier, and James P Kercher. "Controlling tunnelling in methane loss from acetone ions by deuteration". In: *Physical Chemistry Chemical Physics* 17.43 (2015), pp. 28505–28509.

[34] Smriti Anand, Muhannad M Zamari, Getahun Menkir, Robert J Levis, and H Bernhard Schlegel. "Fragmentation pathways in a series of CH3COX molecules in the strong field regime". In: *The Journal of Physical Chemistry A* 108.15 (2004), pp. 3162–3165.

List of Figures

List of Tables

Listings

Danksagung

Zum Ende des mit Abstand lehrreichsten Jahres meines Lebens und nach über fünf Jahren Studium möchte ich mich bei unzähligen, besonderen Menschen bedanken, ohne die diese Arbeit nicht möglich gewesen wäre und deren moralische und fachliche Unterstützung einen wertvollen Beitrag geliefert haben.

Mein besonderer Dank gebührt dem Betreuer meiner Masterarbeit, Ass.Prof. Dr. Markus Koch, dessen umfassende Betreuung immer sehr lehrreich und genau im richtigen Maße fordernd war. Unzählige Diskussionen und geduldige Erklärungen, die einem immer das Gefühl gaben auf Augenhöhe zu agieren, prägten ein sehr harmonisches Gruppenumfeld und erzeugten eine motivierende Atmosphäre, die einem den Ansporn gab sich immer wieder für komplizierte physikalische Fragestellungen zu begeistern.

Meinem Laborkollegen Pascal Heim möchte ich mich für die entspannte und freundschaftliche Atmosphäre des letzten Jahres bedanken, welche die vielen gemeinsamen Stunden im (oft abgedunkelten) Labor zu einer angenehmen, lehrreichen Erfahrung gemacht hat. Auch von seinen profunden Programmier-Kenntnissen und seiner physikalischer Kompetenz konnte ich im Laufe des Jahres sehr profitieren und lernen.

Für die Möglichkeit am Institut für Experimentalphysik meine Masterarbeit zu verfassen bedanke ich mich bei Univ. Prof. Dr. Wolfgang E. Ernst.

Für die reibungslose Einschulung im Labor möchte ich mich bei Paul Maierhofer und Markus Bainschab bedanken. Ebenso danke ich meinen langjährigen Studien-, und nun auch Laborkollegen, Sascha Ranftl und Stefan Cesnik, für die gute Zusammenarbeit, sie alle haben Verantwortung für das immer angenehme Ambiente im Büro. Zu erwähnen ist auch das allgemein hervorragende Klima am Institut für Experimentalphysik, für das alle Kollegen der Forschungsgruppe, sei es beim all-wöchentlichen kulinarischen Genuss von Barilla-Spezialitäten oder bei der einen oder anderen Kaffeepause zwischendurch, verantwortlich sind.

Nun am Ende von fünf Jahren Studium freut es mich eine Reihe von Studienkollegen seit langem auch gute Freunde nennen zu dürfen, die bei unzähligen gemeinsamen Abenden, sei es beim Lernen, beim Rechnen von Übungszetteln, beim Verfassen von Protokollen oder beim Erstellen von Programmen einen wertvollen Beitrag zu einer angenehmen Studienzeit lieferten. Neben den bereits erwähnten Herren Cesnik und Ranftl möchte ich mich noch namentlich bei meinem langjährigen Labor- und Programmierpartner Andreas Jeindl, sowie Lukas Hörmann bedanken. Viele weitere hatten Anteil an einem entspannten Studienleben, die ich nicht alle zu nennen vermag.

Für moralischen Rückhalt sorgten stets ein weiter Kreis von guten Freunden aus meiner Heimatstadt Hartberg, denen ich dafür meinen Dank ausspreche.

Für die nicht nur finanzielle, sondern auch großartige moralische Unterstützung möchte ich mich bei meinen Eltern Birgit und Horst und deren Partnern bedanken, die mir ermöglicht haben den von mir gewählten Bildungsweg selbstständig und ohne Druck zu gehen. Danke auch an meine Schwester Elisabeth und alle Verwandten und Schwieger-Verwandten, die mir immer den nötigen Halt und Zuspruch gewährten.

Zu guter Letzt danke ich dir, Barbara, für deine immer währende Unterstützung, dein Verständnis für lange Lernnächte und für den starken Rückhalt, den ich stets durch dich erfahre.

Graz, März 2017 Bernhard Thaler